



OPEN Unraveling the structure–activity relationships of organometallic ferrocene-pyrazole and ferrocene-pyrimidine curcumin analogues in amyloid- β aggregation and glioblastoma treatment

Veronika Kovač^{1,8}, Veronika Huntosova^{2,3,8}, Viktória Fedorova⁴, Nikitas Georgiou^{2,5}, Jian-Zong Lai⁶, Fan-Ching Chien⁶, Shean-Jen Chen⁷, Filip Dolenec¹ & Katarina Siposova⁴✉

Neurodegenerative and oncological disorders, such as Alzheimer's disease (AD) and glioblastoma (GBM), are major global health challenges. Recent evidence indicates shared molecular mechanisms between these diseases, including dysregulated oxidative stress, mitochondrial dysfunction, and protein aggregation. We hypothesized that ferrocene-containing curcumin derivatives could exert dual-functional effects by simultaneously modulating amyloid- β (A β) aggregation and inhibiting glioblastoma cell proliferation. This study explores organometallic ferrocene compounds linked to four pyrazole and two pyrimidine analogues of curcumin with different substituents for their effects on amyloid- β -peptide (A β) aggregation and glioblastoma. To test this, pyrazole (FcPy-Cur-H, FcPy-Cur-COPh, FcPy-Cur-COFc, FcPy-Cur-Me) and pyrimidine (FcPyn-Cur-O, FcPyn-Cur-S) analogues were synthesized and evaluated. Thioflavin T fluorescence, atomic force microscopy, and single-molecule localization microscopy revealed structure-dependent inhibition of A β fibrillogenesis, with FcPyn-Cur-O, FcPyn-Cur-S, and FcPy-Cur-H showing the strongest anti-amyloidogenic activity. Concurrently, these derivatives reduced U87MG glioblastoma cell viability in a dose-dependent manner, inducing apoptotic features, mitochondrial disruption, and α -tubulin destabilization. Our results demonstrate that specific structural modifications of ferrocene-curcumin analogues enhance their dual anti-amyloidogenic and anticancer activities, highlighting the therapeutic potential of multifunctional compounds. This study provides a conceptual advance by combining neurodegenerative and oncological targets within a single chemical framework, offering a promising strategy for the development of multitargeted therapeutics for complex brain disorders.

Keywords Ferrocenyl-pyrazole/pyrimidine-curcumin derivatives, Amyloid aggregation, Glioblastoma

Aging is characterized by a decline in the body's ability to repair and regenerate tissues and organs, making them more susceptible to damage and less capable of recovery. This natural process unfolds over time in all living organisms and manifests at multiple biological levels, molecular, cellular, tissue, and systemic, under the

¹Laboratory of Organic Chemistry, Faculty of Food Technology and Biotechnology, University of Zagreb, Pierotti Str. 6, Zagreb, Croatia. ²Center for Interdisciplinary Biosciences, Technology and Innovation Park, P.J. Safarik University in Kosice, Jesenna 5, Kosice, Slovakia. ³Institute of Animal Biochemistry and Genetics, Centre of Biosciences, Slovak Academy of Sciences, Dúbravská cesta 9, Bratislava, Slovakia. ⁴Department of Biophysics, Institute of Experimental Physics, Slovak Academy of Sciences, Watsonova 47, Kosice, Slovakia. ⁵Laboratory of Organic Chemistry, Department of Chemistry, National and Kapodistrian University of Athens, Panepistimioupolis Zografou, 11571 Athens, Greece. ⁶Department of Optics and Photonics, National Central University, No. 300, Zhongda Rd., Zhongli District, Taoyuan 32001, Taiwan, R.O.C.. ⁷College of Photonics, National Yang Ming Chiao Tung University, Gaofa 3rd Rd., Guiren District, Tainan 71150, Taiwan, R.O.C.. ⁸Veronika Kovač and Veronika Huntosova contributed equally to this work. ✉email: siposova@saske.sk

influence of genetic, epigenetic, and environmental factors¹. Current advances in medicine and technology have significantly extended human life expectancy, leading to a global rise in the ageing population. However, this demographic shift is accompanied by an increasing prevalence of age-related conditions such as dementia. According to the World Health Organization (WHO), someone in the world develops dementia every three seconds. As of 2020, over 55 million individuals are living with dementia worldwide, a number projected to nearly triple by 2050. Dementia, as defined by the WHO, is a chronic syndrome characterized by a spectrum of cognitive and behavioral impairments. It is caused by progressive deterioration of neuronal cells and their networks, particularly in the brain. Dementia is also closely associated with the ageing process². Among the plethora of various neurodegenerative disorders and dementia, Alzheimer's disease (AD) is the most prevalent, accounting for 50–60% of all cases^{3–5}. The pathogenesis and etiology of AD are multifactorial and remain incompletely understood. Numerous hypotheses and molecular targets have been proposed to explain its onset and progression. Apart from the observable cognitive decline, AD is defined by two key pathological markers in brain tissue. These include extracellular amyloid-beta ($A\beta$) plaques and intracellular neurofibrillary tangles formed by hyperphosphorylated tau protein^{6–9}. These insoluble and densely packed aggregates are considered central to the disease's development and are associated with neurotoxic effects that disrupt normal neuronal function. The accumulation of misfolded proteins such as oligomeric $A\beta$ and tau tangles in the central nervous system contributes significantly to the neurodegenerative cascade observed in AD^{7,10–13}. This biochemical complexity poses a major obstacle in the search for effective therapeutic strategies. Thus, gaining a deeper understanding of the molecular principles governing protein misfolding and aggregation is critical for the development of targeted interventions^{14–16}. Considerable research efforts have focused on discovering molecules that can inhibit $A\beta$ production, promote its clearance, or prevent its aggregation. Strategies designed to impede fibril formation or to disassemble existing aggregates have shown promise. Successful inhibition requires disruption of the intermolecular forces that drive $A\beta$ self-assembly into toxic fibrils and oligomers. The effectiveness of this process depends strongly on the chemical properties of the inhibitors. Despite significant progress, no low-molecular-weight compound with robust efficacy against amyloid aggregation has yet been approved for clinical use.

On the other hand, glioblastoma multiforme (GBM) is the most common primary brain tumor in adults, characterized by high invasiveness, rapid growth and poor prognosis. It is still one of the most difficult malignant diseases worldwide¹⁷. Although the AD and GBM are both complex neurological diseases with different pathologies, the rationale for investigating both Alzheimer's disease and glioblastoma in a single study is based on emerging evidence of shared molecular and cellular mechanisms. Both AD and GBM exhibit dysregulation of oxidative stress and mitochondrial function, which contribute to neuronal loss in AD and promote proliferation and survival of tumor cells in GBM. Abnormal protein aggregation, a hallmark of AD pathology, has also been implicated in the modulation of cell behavior, including proliferation and migration and is in close connection to glioblastoma and oxidative stress as well. Furthermore, chronic neuroinflammation and immune dysregulation are common features of both diseases, influencing disease progression and cellular microenvironment. Alterations in autophagy and key signaling pathways, such as PI3K/AKT/mTOR and Wnt signaling pathway, further support the overlap of pathophysiological processes^{18–23}.

Both glioblastoma and dementia, including AD are devastating diseases with limited treatments that are usually not curative. Curcumin has garnered significant interest for its ability to inhibit protein amyloid fibrillation, a key process implicated in neurodegenerative diseases. In addition, Curcumin derivatives have been shown to inhibit glioblastoma cell proliferation and suppress mitochondrial metabolism^{18–20}. Despite this, its therapeutic potential is hindered by poor chemical stability under physiological conditions, largely attributed to the β -diketone moiety, which also contributes to its low bioavailability. To address these limitations, structural modification has become a crucial strategy to enhance both stability and pharmacological efficacy. In particular, analogues that eliminate the β -diketone group, a known factor in curcumin's rapid degradation, have been synthesized and often retain or even surpass the biological activity of the parent compound^{24,25}. Among these, heterocyclic derivatives have shown especially promising potential in the diagnosis and treatment of Alzheimer's disease, prompting extensive research efforts^{26–28}.

In addition, more attention has been paid to metallodrugs in biological and medicinal chemistry in recent decades^{29,30}. Ferrocene as a stable metallocene compound is the most commonly used organometallic component for introduction into organic and bioinorganic pharmaceuticals for the treatment of various diseases such as cancer, malaria or bacterial and fungal infections^{31,32}. Among others, it was found that this type of modification with ferrocene imparts specific properties to the molecules, such as increasing lipophilicity, significantly reducing toxicity, improving the ability to cross the blood-brain barrier or imparting ideal electrochemical properties³³.

Only a limited number of studies have explored ferrocene derivatives as modulators of amyloid aggregation^{34–37} or ferrocene-based compounds with anti-glioblastoma activity^{38–42}, but never have both activities been investigated in a single study. Motivated by this, a series of *ferrocene-containing pyrazole* derivatives were recently resynthesized using an improved method to increase yields. These compounds include FcPy-Cur-H, FcPy-Cur-COPh, FcPy-Cur-COFc, and FcPy-Cur-Me, where Fc = ferrocene, Py = pyrazole, Cur = curcumin, and H, COPh, COFc, and Me indicate specific modifications of the pyrazole moiety. In addition, new *pyrimidine analogues* of curcumin have been synthesized and evaluated. These include FcPyn-Cur-O and FcPyn-Cur-S, where -O and -S correspond to modifications of the pyrimidine moiety. The goal of these syntheses was to enhance the compounds' ability to modulate amyloid aggregation and inhibit glioblastoma cell growth⁴³. In this study, a range of experimental methods was employed to investigate the amyloid aggregation of $A\beta$ peptide in the presence of newly synthesized compounds. Our results demonstrate that ferrocene-containing curcumin derivatives can simultaneously modulate $A\beta$ aggregation and inhibit glioblastoma cell proliferation, reflecting emerging evidence of shared molecular mechanisms between Alzheimer's disease and glioblastoma. Furthermore, their efficacy appears to be structure-dependent, with specific modifications of the pyrazole and pyrimidine moieties

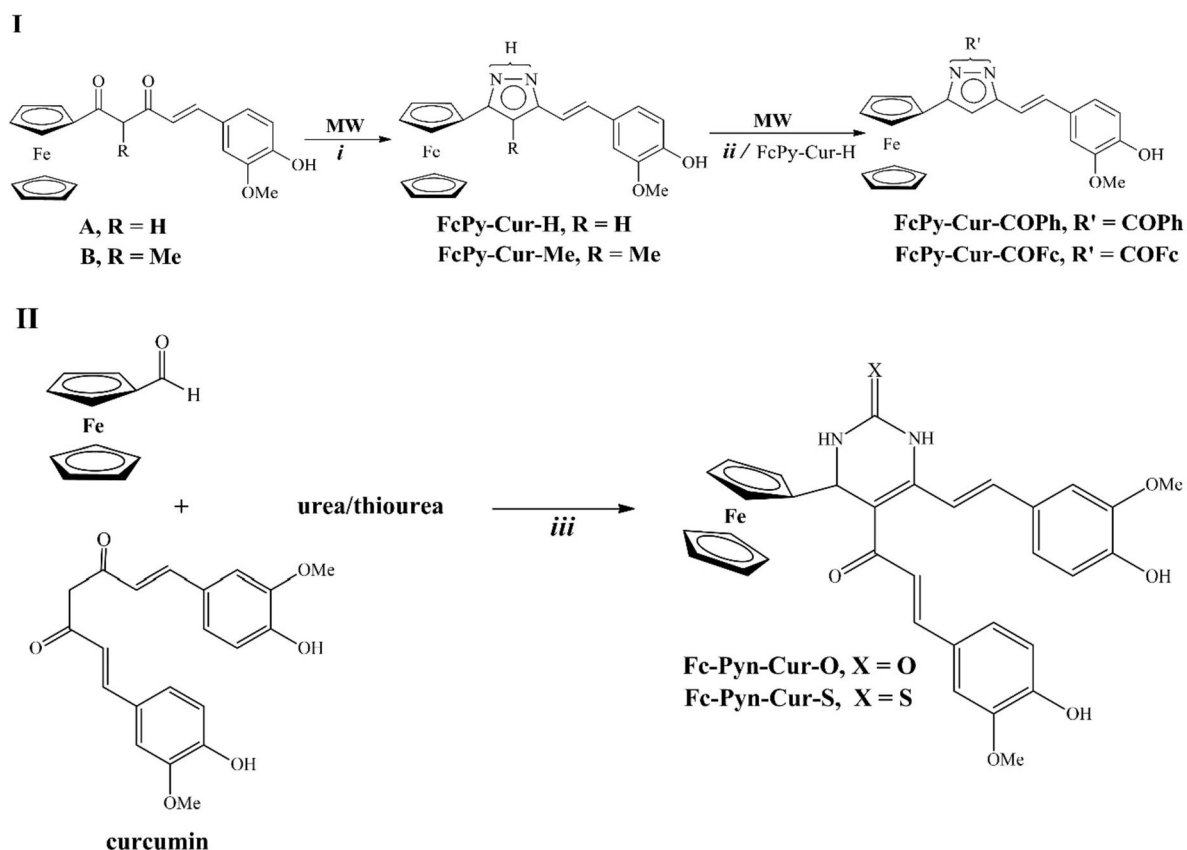


Fig. 1. Synthetic pathway of **(I)** ferrocene-containing pyrazole analogues of curcumin **FcPy-Cur-H**, **FcPy-Cur-Me**, **FcPy-Cur-COPh**, **FcPy-Cur-COFc** and **(II)** ferrocene-containing pyrimidin-2-one (thione) derivatives of curcumin **FcPyn-Cur-O** and **FcPyn-Cur-S**. **(i)** $\text{NH}_2\text{NH}_2 \cdot \text{H}_2\text{O}$ / AcOH , microwave irradiation. **(ii)** PhCOCl or FcCOCl / dichloroethane/ microwave irradiation; Fc = ferrocenyl. **(iii)** dry THF, piperidine, 80°C .

Comp.	Duration of reaction		Yield of reaction (%)	
	Conventional [†]	Microwave	Conventional [†]	Microwave
FcPy-Cur-H	24 h	20 min	50	67
FcPy-Cur-Me	24 h	40 min	48	65
FcPy-Cur-COPh	4 h	30 min	47	69
FcPy-Cur-COFc	4 h	45 min	33	52

Table 1. Comparison of the duration and yields of reactions to obtain ferrocene-containing pyrazole analogues of Curcumin by conventional chemical synthesis and microwave synthesis. [[†] 43].

enhancing both anti-amyloidogenic and anticancer activities. This dual functionality positions these compounds as promising candidates for the development of multifunctional therapeutics targeting both neurodegenerative and malignant brain disorders.

Results and discussion

Chemistry

The synthesis pathway of the ferrocene-containing pyrazole **FcPy-Cur-H**, **FcPy-Cur-Me**, **FcPy-Cur-COPh**, **FcPy-Cur-COFc** and pyrimidin-2-one (thione) **FcPyn-Cur-O**, **FcPyn-Cur-S** derivatives of curcumin is shown in Fig. 1.

In our previous work, we reported the preparation of ferrocene-containing pyrazole analogues of curcumin using conventional synthetic methods⁴³. Since the yields of these reactions were below 50%, we explored microwave-assisted synthesis to improve reaction efficiency. The reactions were carried out at 50 – 90°C , resulting in shorter reaction times and higher yields compared to conventional methods (e.g., reduction from 24 h to 20 min and increase in yield from 50% to 67% for **FcPy-Cur-H**, Table 1). The chemical structures of compounds

were confirmed by FT-IR, ^1H and ^{13}C NMR spectroscopy and by ESI-MS spectrometry, with all spectra provided in the Supplementary Information.

New ferrocenyl pyrimidin-2-one **FcPyn-Cur-O** and pyrimidin-2-thione **FcPyn-Cur-S** derivatives of curcumin were synthesized via a one-pot multicomponent Biginelli reaction leading to the formation of nitrogen-containing six-membered heterocycles. Curcumin, ferrocene-carboxaldehyde, urea/thiourea and a catalytic amount of piperidine in tetrahydrofuran were heated under reflux for 48 h, and after TLC purification in ethyl acetate/hexane mixture, **FcPyn-Cur-O** and **FcPyn-Cur-S** were obtained in yields of 29% and 25%, respectively. In the IR spectra of the dichloromethane solutions of **FcPyn-Cur-O** and **FcPyn-Cur-S**, the absorption bands of the phenolic O-H and N-H stretching vibrations are visible as weak singlets at 3524 cm^{-1} and 3415 cm^{-1} , respectively. The band as a strong singlet at about 1594 cm^{-1} confirms the presence of the C=O carbonyl group, and the bending vibration of the N-H group showed the band at 1514 cm^{-1} . The detailed ^1H and ^{13}C NMR assignments for **FcPyn-Cur-O** and **FcPyn-Cur-S** can be found in the Supplementary Information (Table 2 and all NMR spectra).

Since two-dimensional NMR spectroscopic experiments provide more detailed structural information, COSY, HMBC and HSQC NMR spectra of **FcPyn-Cur-O** were also performed to support the assignment of the signals (Figure S17–S19 in the Supplementary Information). The ^1H – ^1H 2D COSY spectra show cross-peaks only for directly coupled protons, the ^1H – ^{13}C 2D HMBC provides correlations between protons and carbons that are two or three bonds apart (although occasionally correlations with four or even five bonds can be observed), and the ^1H – ^{13}C 2D HSQC spectrum correlates the chemical shifts of ^1H and ^{13}C nuclei that are directly bonded⁴⁴. All NMR spectra as well as the ESI-MS spectra of the new compounds **FcPyn-Cur-O** and **FcPyn-Cur-S** were consistent with the proposed structures.

Molecular docking calculations

Molecular docking calculations were performed to explore potential interactions of the compounds with Amyloid beta peptide (1–40) ($\text{A}\beta_{1-40}$) (Fig. 2). The same grid parameters were used for all the compounds: $X=80$, $Y=92$, $Z=40$ and dot spacing 0.375 \AA (default). The calculated binding energy scores are reported in Table 2.

Compounds **FcPy-Cur-COPh** and **FcPy-Cur-COFc** showed the lowest (the most favourable) binding energies (-7.80 and -7.81 kcal/mol , respectively), suggesting relatively stronger interactions with the target protein compared to the other analogues. In contrast, compounds **FcPyn-Cur-O** and **FcPyn-Cur-S** showed higher binding energies (above -6.50 kcal/mol) indicating potentially weaker or less optimal interactions. All compounds were predicted to interact within the substrate-binding cleft, forming hydrogen bonds and hydrophobic interactions with key residues. Docking results suggest that **FcPy-Cur-COPh** and **FcPy-Cur-COFc** form stabilizing interactions with residues LEU17, PHE19, and ASP23, along with favorable π - π stacking with PHE20 (-7.80 and -7.81 kcal/mol , respectively). Compound **FcPy-Cur-Me** forms hydrogen bonds with SER26 and ASP23, consistent with its moderately favourable binding energy.

In contrast, compounds **FcPyn-Cur-O** and **FcPyn-Cur-S**, which exhibited higher (less favorable) binding energies, showed weaker or less extensive interactions, particularly with GLU22 and PHE19, which may contribute to their relatively lower predicted stability within the binding site. Curcumin, by comparison, binds within the $\text{A}\beta_{1-40}$ but interacts mainly with LYS16, GLN15, and PHE20, forming fewer hydrogen bonds and hydrophobic contacts than **FcPy-Cur-COPh** and **FcPy-Cur-COFc**, and lacking key interactions with ASP23 and PHE19⁴⁵. Overall, the docking results suggest that the examined ferrocene-containing compounds adopt more specific binding modes than curcumin. It should be noted that rigid docking does not account for the conformational flexibility of $\text{A}\beta$ or its dynamic aggregation process. This limitation likely explains the discrepancy between the docking scores and the experimental IC_{50} values, where **FcPyn-Cur-O** and **FcPyn-Cur-S** were the most effective inhibitors despite less favorable docking energies. Therefore, the docking data are best interpreted as qualitative illustrations that complement the experimental structure-activity relationships, rather than as precise quantitative predictors of inhibitory potency.

Evaluation of anti-amyloid activity of ferrocene-containing analogues

The strategy to evaluate the effects of the newly synthesized ferrocene-containing curcumin analogues on $\text{A}\beta_{1-40}$ peptide fibrillogenesis involved concentration- and time-dependent analyses. Amyloid formation was monitored using the thioflavin T (ThT) fluorescence assay, a widely accepted technique based on the principle that the presence of fibrils increases ThT fluorescence, whereas a reduction in fibril content results in decreased fluorescence^{46–49}.

Compound	Binding energy (kcal/mol)
(FcPy-Cur-H)	-6.95
(FcPy-Cur-COPh)	-7.80
(FcPy-Cur-COFc)	-7.81
(FcPy-Cur-Me)	-6.87
(FcPyn-Cur-O)	-6.65
(FcPyn-Cur-S)	-6.48

Table 2. Docking score denoted as binding energy calculated for studied compounds with $\text{A}\beta_{1-40}$.

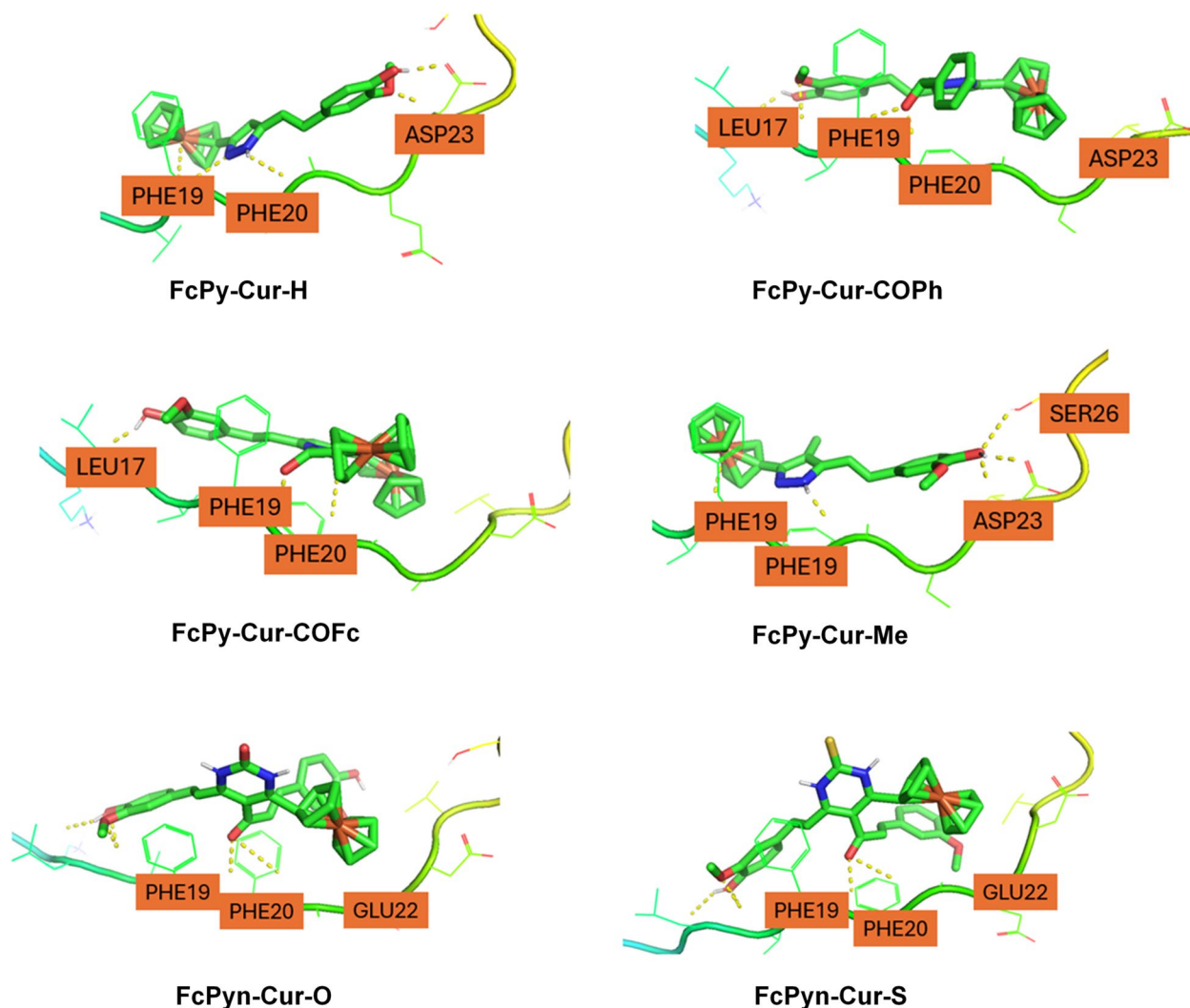


Fig. 2. The binding modes of ferrocene-containing analogues of curcumin to A β_{1-40} peptide.

Concentration-dependent assays were performed using a fixed A β_{1-40} peptide concentration of 25 μ M in 150 mM MOPS buffer at pH 6.9. Figure 3 shows the relative ThT fluorescence intensities of A β_{1-40} incubated with increasing concentrations (0.05 μ M to 1 mM) of pyrazole-derivatives (**FcPy-Cur-H**, **FcPy-Cur-COPh**, **FcPy-Cur-COFc**, **FcPy-Cur-Me**; Fig. 3A) and pyrimidine-derivatives (**FcPyn-Cur-O**, **FcPyn-Cur-S**; Fig. 3B). Relative fluorescence intensity was quantified by normalizing the ThT signal of untreated amyloid fibrils (defined as 100%) against the signal following the treatment with ferrocene-containing curcumin analogues. At the lowest submicromolar analogue concentrations (0.05 and 0.1 μ M), no significant effect on A β_{1-40} fibril formation was observed, with ThT fluorescence remaining comparable to untreated controls. Increasing analogue concentrations resulted in a concentration-dependent attenuation of ThT fluorescence, consistent with inhibited amyloid formation. Experimental data were fitted using four-parameter sigmoidal models to characterize the dose-response relationships.

The potential for disassembly of preformed A β_{1-40} fibrils was subsequently evaluated by incubating aggregates with the compounds for 24 h (Fig. 3C and D). Both inhibition of fibril formation and disassembly of pre-existing fibrils by **FcPy-Cur-H**, **FcPy-Cur-COPh**, **FcPy-Cur-COFc**, **FcPy-Cur-Me**, **FcPyn-Cur-O**, and **FcPyn-Cur-S** exhibited dose dependency, reflected in sigmoidal declines in ThT fluorescence (Fig. 3). These measurements allowed the determination of half-maximal inhibitory (IC_{50}) and disassembly (DC_{50}) concentrations for each analogue. IC_{50} values ranged approximately from 4 to 30 μ M, while DC_{50} values varied between roughly 9 and 70 μ M (Table 3). A structure-dependent trend was observed, with pyrimidine derivatives **FcPyn-Cur-O** and **FcPyn-Cur-S** exhibiting the most pronounced inhibitory activity. Notably, DC_{50} values were largely consistent across compounds (~9–20 μ M), except for the pyrazole derivative **FcPy-Cur-COFc**, which exhibited a higher DC_{50} (70 μ M), indicating comparatively weaker disassembly activity.

Inhibition of A β aggregation by small molecules is generally mediated through disruption of intermolecular forces driving fibril formation, including electrostatic interactions, hydrogen bonding, π - π stacking, and van der Waals forces involving specific peptide residues^{50,51}. The ferrocene-containing curcumin analogues possess highly conjugated systems with π -electron delocalization, dual aromatic moieties bridged by rigid linkers (8–16

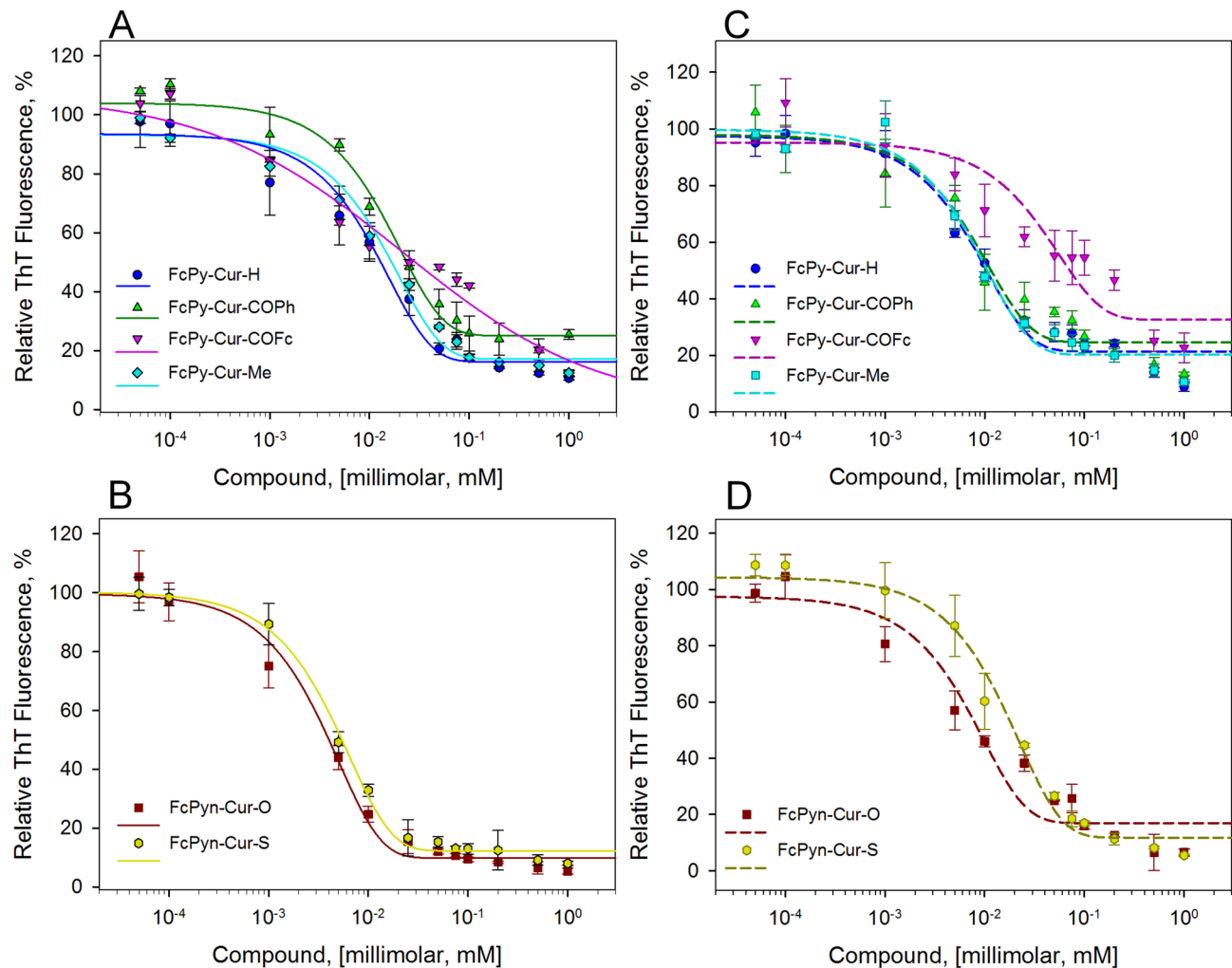


Fig. 3. Concentration-dependent effects of ferrocene-containing analogues of curcumin on $A\beta_{1-40}$ peptide amyloid aggregates formation monitored via ThT fluorescence assay. A- ferrocene-containing pyrazole analogues of curcumin-induced inhibition of $A\beta_{1-40}$ peptide fibrillization. B- ferrocene-containing pyrimidine analogues of curcumin-induced inhibition of $A\beta_{1-40}$ peptide fibrillization. C- ferrocene-containing pyrazole analogues of curcumin-induced disassembly of $A\beta_{1-40}$ fibrils. D- ferrocene-containing pyrimidine analogues of curcumin-induced disassembly of $A\beta_{1-40}$ fibrils. The anti-amyloidogenic effect was quantified as a function of ferrocene-containing analogues of curcumin concentrations ranging from 0.05–1 mM concentration at a fixed 25 μ M concentration of $A\beta_{1-40}$ peptide/fibrils. The ThT fluorescence intensities of ferrocene-containing analogues of curcumin-containing samples were normalized to fluorescence intensities recorded for control samples ($A\beta_{1-40}$ fibrils alone; taken as 100%). Each experiment was performed five times; error bars represent the average deviation for repeated measurements of five separate samples.

Curcumin analogues		Anti-amyloid activity in [μ M]	
		Inhibiting IC_{50}	Disassembly DC_{50}
Ferrocene-containing PYRAZOLE	FcPy-Cur-H	13 \pm 1	10.4 \pm 0.65
	FcPy-Cur-COPh	23.5 \pm 1.15	12 \pm 1
	FcPy-Cur-COFc	30 \pm 2.0	70 \pm 7
	FcPy-Cur-Me	16.6 \pm 0.9	10.8 \pm 0.7
Ferrocene-containing PYRIMIDINE	FcPyn-Cur-O	4.0 \pm 0.2	8.7 \pm 0.8
	FcPyn-Cur-S	5.5 \pm 0.15	20 \pm 1.1

Table 3. Experimentally determined IC_{50} and DC_{50} values of the studied ferrocene-containing analogues of curcumin.

Å), and hydroxyl or other polar substituents. These features appear critical for effective interactions with A β fibrils^{50,52}.

FcPy-Cur-H, **FcPy-Cur-COPh**, **FcPy-Cur-COFc** and **FcPy-Cur-Me** contain a rigid linker between the ferrocene and benzene rings (<8 Å) and a substituted *p*-hydroxyl group on the benzene ring. Their aromatic nature suggests the potential for π - π stacking interactions with aromatic amino acids in the A β ₁₋₄₀ peptide. Additionally, **FcPy-Cur-H** and **FcPy-Cur-Me** possess two hydrogen bond donors (pyrazole-NH and phenol-OH), enabling stronger interactions with the peptide (IC₅₀ 13 μ M for **FcPy-Cur-H** and 16.6 μ M for **FcPy-Cur-Me**). Introduction of bulky acyl substituents, COPh or COFc at the pyrazole nitrogen reduced anti-aggregating effects (IC₅₀ value for **FcPy-Cur-COPh** and **FcPy-Cur-COFc** was 23.5 μ M and 30 μ M, respectively). The higher DC₅₀ observed for **FcPy-Cur-COFc** (DC₅₀ value of 70 μ M) may be due to steric hindrance limiting interactions with the peptide backbone.

The pyrimidine derivatives **FcPyn-Cur-O** and **FcPyn-Cur-S** feature highly conjugated moieties with two benzene rings connected by rigid linkers (11 Å) and peripheral hydroxyl groups. They satisfy previously described structural criteria for inhibition of A β aggregation⁵⁰ and displayed the highest inhibitory potential in our assays (IC₅₀ 4.0 μ M and 5.5 μ M, respectively). Although docking studies did not predict these molecules as the strongest binders, their ferrocene and dual benzene units likely enhance π - π stacking, while four hydrogen bond donors (two pyrimidine NH and two phenolic OH groups) enable robust interactions with the A β backbone. These interactions may collectively impede fibril formation and promote disassembly, in line with previous hypotheses on multi-site molecular clamps, as previously postulated for porphyrin-based inhibitors^{53,54}. The importance of aromatic rings and π - π stacking for anti-amyloid activity has been documented for various natural and synthetic compounds, including curcumin and its derivatives^{45,54,55}.

Atomic force microscopy (AFM) was used to confirm the results obtained from the ThT fluorescence assay and to reveal the morphology of fibrils. AFM images of fibrils and the effects of curcumin derivatives are shown in Fig. 4. The disassembly process is denoted as “DisA,” and the inhibition process as “Inh,” both visualized at a 10 μ M concentration of the studied compounds. AFM images demonstrated that the presence of ferrocene-containing curcumin derivatives markedly affected the amount and morphology of fibrils formed by A β ₁₋₄₀. Moreover, curcumin derivatives were capable of disassembling pre-formed fibrils. AFM images of the A β ₁₋₄₀ fibrils in the absence of curcumin derivatives showed fibrils displayed the characteristic amyloid morphology with a tendency to form fibril clusters (Fig. 4, control). In contrast, under the same experimental conditions, the presence of ferrocene-containing analogues of curcumin reduced both the size and the number of fibrils. In samples containing pre-formed fibrils, ferrocene-containing curcumin derivatives induced fibril disassembly. Both inhibition and disassembly effects were concentration-dependent.

To obtain more detailed information, single-molecule microscopy (SMLM) was employed. Figure 5 shows the SMLM and summed fluorescence images of the A β fibrils in the absence and presence of the **FcPyn-Cur-S** treatment. The SMLM images of the A β fibrils with a localization precision of 9 \pm 3 nm, revealed distinct fibril morphology compared with summed fluorescence images (Fig. 5, upper and lower panels). Under **FcPyn-Cur-S** treatment at concentrations of 20 and 100 μ M, a reduction in the number of longer A β fibrils was observed in SMLM images, which was less evident in conventional summed fluorescence images. To further quantify this effect, fibril lengths in SMLM images were analyzed statistically. The average lengths of the A β fibril after treatment with 0, 20, and 100 μ M **FcPyn-Cur-S** were 1.64 \pm 0.74, 1.28 \pm 0.64, and 0.55 \pm 0.29 μ m, respectively, (Fig. 6), based on measurements of over 800 fibrils. These results suggest a trend toward shorter fibrils with increasing **FcPyn-Cur-S** concentrations. It should be noted, that these experiments were performed under in vitro conditions, and the observed effects may not fully translate to in vivo systems. AFM and SMLM provide qualitative and semi-quantitative insights, but precise molecular mechanisms and dynamic processes of fibril aggregation and disassembly cannot be fully captured. Further studies are needed to evaluate the effects in physiologically relevant models.

The anticancer activity of ferrocene-containing analogues of curcumin

The anticancer activity of ferrocene-containing analogues of curcumin was investigated in U87MG cancer cells. The uptake of ferrocene-containing analogues of curcumin was evaluated by flow cytometry. Figure 7A shows the distribution plots in two spectral ranges (V525 and B525), where apoptosis (B525) was detected. Quantification of fluorescence revealed weak fluorescence signals for **FcPy-Cur-H**, **FcPy-Cur-COPh**, **FcPy-Cur-COFc** and **FcPy-Cur-Me**, with intensities below the autofluorescence of U87MG cells. In contrast, stronger fluorescence was observed for **FcPyn-Cur-O** and **FcPyn-Cur-S**. Microscopic imaging of **FcPyn-Cur-S** confirmed this observation, showing the homogeneous distribution of **FcPyn-Cur-S** fluorescence within the cells (Fig. 7A). This intrinsic fluorescence may interfere with the detection of apoptosis, as it partially overlaps with the fluorescence detection channel of the apoptosis probe. Apoptosis was investigated in U87MG cells exposed to 12.5 μ M ferrocene-containing analogues of curcumin for 24 h. Fluorescence of AnnexinV/FITC, which reflects phosphatidylserine expression in apoptotic cells, was compared with the autofluorescence of the treated cells (Fig. 7B). The correlation plot was divided into four quadrants, with the lower right quadrant representing apoptotic cells (marked with a red rectangle). It should be noted that the overlap of compound fluorescence with the apoptosis probe may affect the precise quantification of apoptotic cells, representing a limitation of this assay.

The upward shift in autofluorescence of **FcPyn-Cur-O** and **FcPyn-Cur-S** (see black marker) was similar to the previous observation for uptake. Under these conditions (**FcPyn-Cur-O** and **FcPyn-Cur-S**), approximately 50% of apoptotic cells were detected, as indicated in the corresponding histograms. These results suggest that the **FcPyn-Cur-O** and **FcPyn-Cur-S** may exert a relatively strong anticancer effect. To further investigate this, the MTT assay was performed. Formazan production was measured in U87MG cells treated with ferrocene-containing analogues of curcumin for 48 h to allow sufficient time for biological activity, following protocols previously applied for **FcPy-Cur-H**, **FcPy-Cur-Me**, **FcPy-Cur-COPh** and **FcPy-Cur-COFc** in hepatocarcinoma,

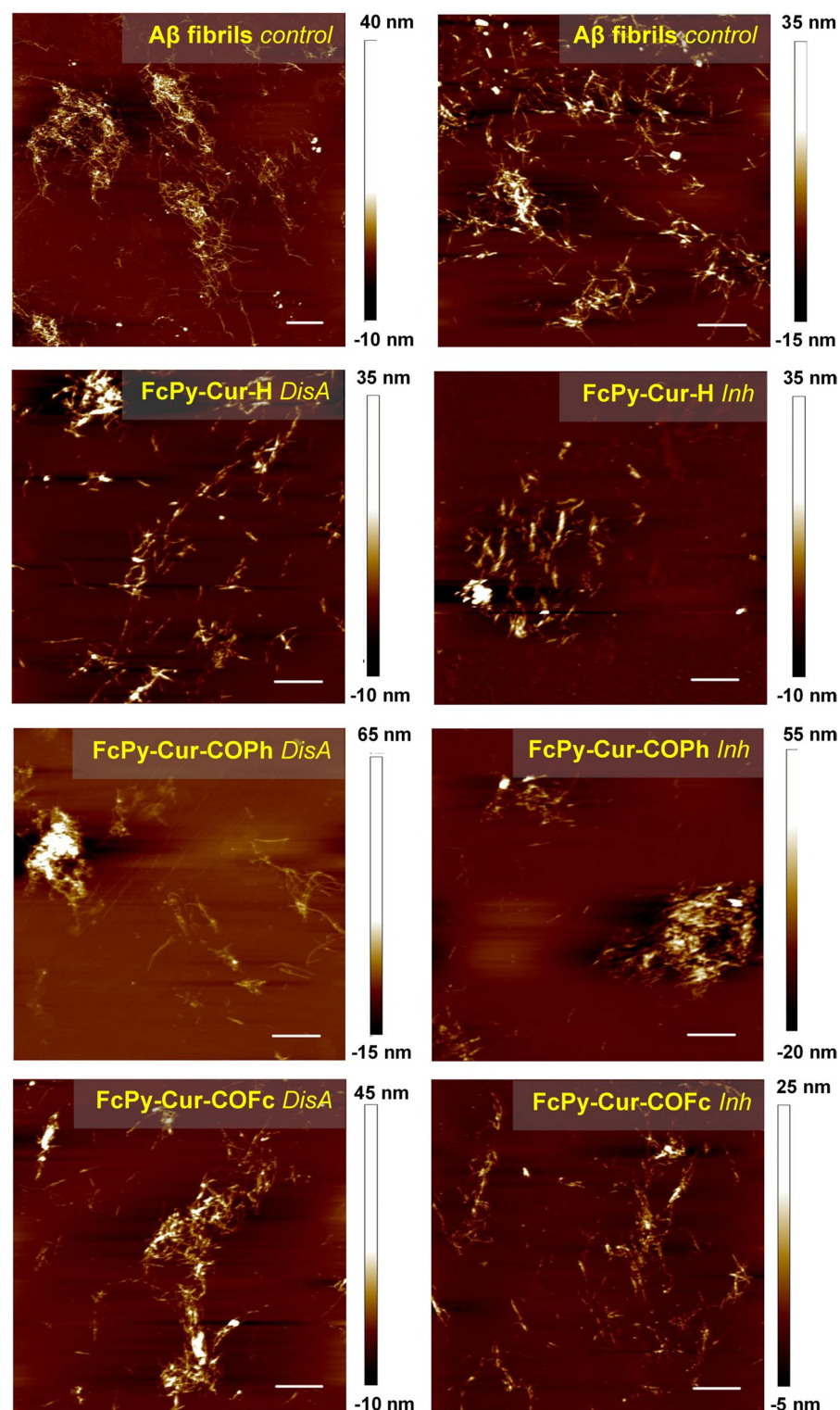


Fig. 4. Atomic force microscopy visualization of pre-formed Aβ₁₋₄₀ fibrils incubated with ferrocene-containing analogues of curcumin (*Disassembly, DisA*) and of Aβ₁₋₄₀ fibrils formed alone (control) and in the presence of ferrocene-containing analogues of curcumin (*Inhibition, Inh*). The data analyses were performed using NanoScope Analysis 1.20 software. Scale bars represent 2 μm and 5 μm (first control AFM scan of Aβ₁₋₄₀ fibrils).

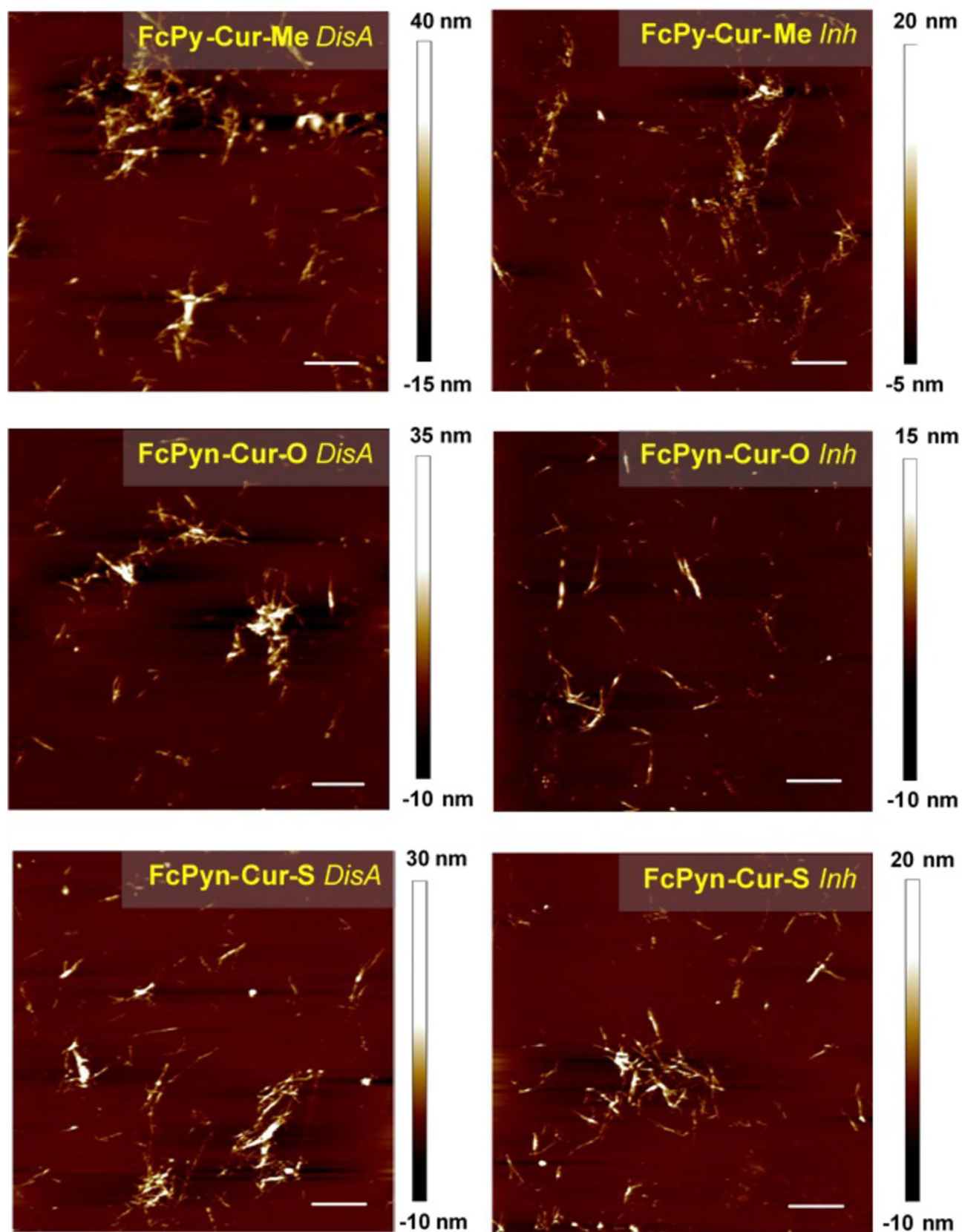


Fig. 4. (continued)

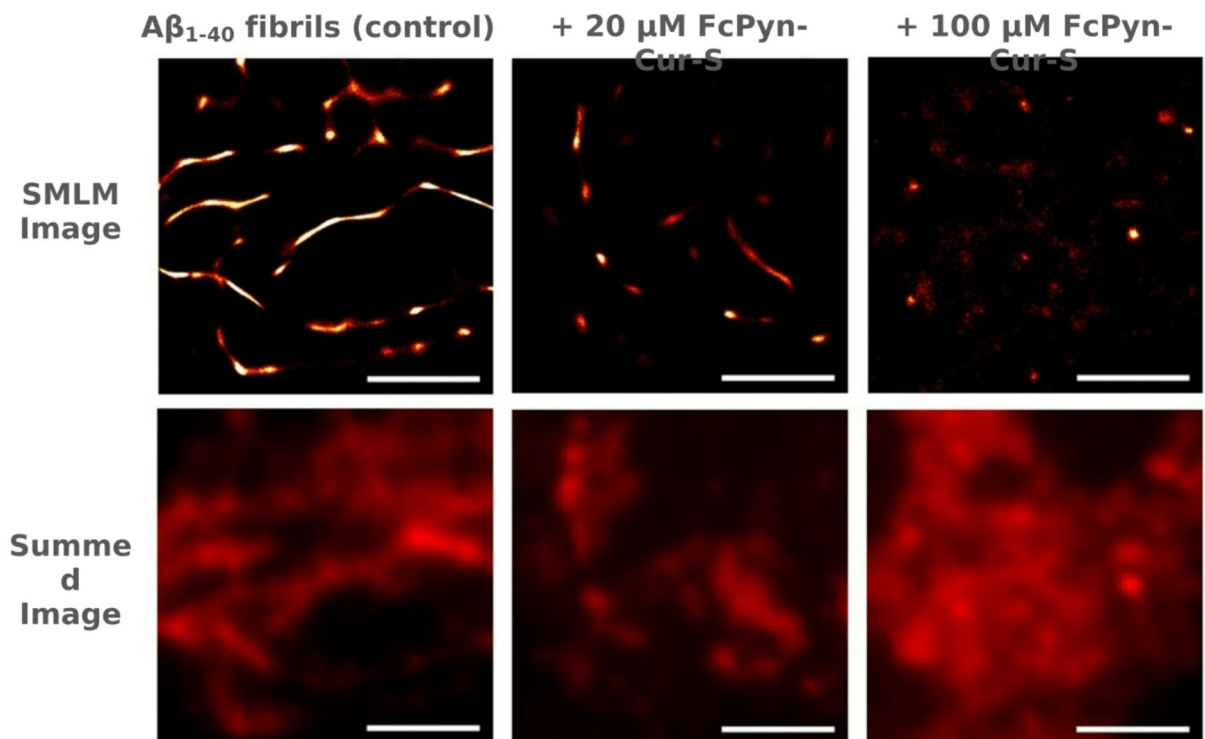


Fig. 5. Single-molecule localization microscopy (SMLM) visualization of pre-formed $A\beta_{1-40}$ fibrils incubated with **FcPyn-Cur-S** (Disassembly). The concentration of deposited $A\beta_{1-40}$ fibrils was $20 \mu\text{M}$. Scale bars represent $2 \mu\text{m}$.

cervical carcinoma and breast cancer cells⁴³. The results of the MTT assay are shown in Fig. 8. A concentration-dependent response of cells to treatment was observed for all ferrocene-containing analogues of curcumin. However, **FcPy-Cur-COPh**, **FcPy-Cur-COFc** and **FcPy-Cur-Me** were less effective at lower concentrations (2.5 – $12.5 \mu\text{M}$). The strongest effects were observed with **FcPyn-Cur-O** and **FcPyn-Cur-S**, where formazan production was reduced to below 60%. A gradual decrease in cell viability was observed after the application of **FcPy-Cur-H**. The inhibition of glioblastoma cell proliferation detected in the present study appeared stronger than previously reported in hepatocarcinoma, cervical carcinoma and breast cancer cells. All tested concentrations were below the IC_{50} values reported for the first four compounds in non-cancerous cells (CHO-K1 and HaCaT)⁴³. In addition, the two newly synthesised compounds are predicted to have IC_{50} below $12.5 \mu\text{M}$. Therefore, morphological microscopy was performed after treatment with $12.5 \mu\text{M}$ concentration of the ferrocene-containing analogues of curcumin to visualize potential differences in their biological effects. It should be noted that differences between cell lines, assay sensitivity, and intrinsic compound fluorescence may influence the interpretation of anticancer effects, and these results should be considered as indicative rather than definitive.

Fluorescence immunostaining was performed to obtain higher resolution and subcellular information on mitochondrial morphology, stability of the Golgi apparatus and the α -tubulin network in U87MG cells during treatment with ferrocene-containing analogues of curcumin. Improved resolution of these subcellular compartments was achieved using the Airyscan detector of the ZEISS confocal fluorescence imaging system. A rich tubulin network (green) is visible in control cells (Fig. 9), with long filaments filling the cell body. Ubiquinol-cytochrome *c* reductase is primarily localized in mitochondria, which appear tubular (orange) in large numbers in the perinuclear region. Clearly defined nuclei (blue) are also visible. Similar patterns to the control were observed in cells exposed to **FcPy-Cur-COPh**, **FcPy-Cur-COFc** and **FcPy-Cur-Me**. In cells treated with **FcPy-Cur-H**, mitochondrial clusters were observed in perinuclear areas (see white arrow in Fig. 9). Morphological changes are evident, although the tubulin network appears largely preserved. These observations are consistent with MTT assay results, where mitochondrial activity was inhibited by approximately 60%. In contrast, complete destabilisation of the tubulin network was observed in cells treated with **FcPyn-Cur-O** and **FcPyn-Cur-S**, with granular mitochondria forming large clusters (see white arrows in Fig. 9). Apoptotic nuclei were identified by condensation of chromatin.

The metabolism of the cell and the de novo synthesis of proteins are dependent on the functionality of the Golgi apparatus. Fluorescence immunostaining of Giantin was performed to examine the Golgi apparatus, a potential target of the compounds. Figure 8 shows mitochondria stained for ubiquinol-cytochrome *c* reductase (orange) and Golgi cisternae stained for Giantin (green), with nuclei visualized using Hoechst. Compact Golgi cisternae were observed in control cells and in cells exposed to **FcPy-Cur-Me**, **FcPy-Cur-COPh** and **FcPy-Cur-COFc**.

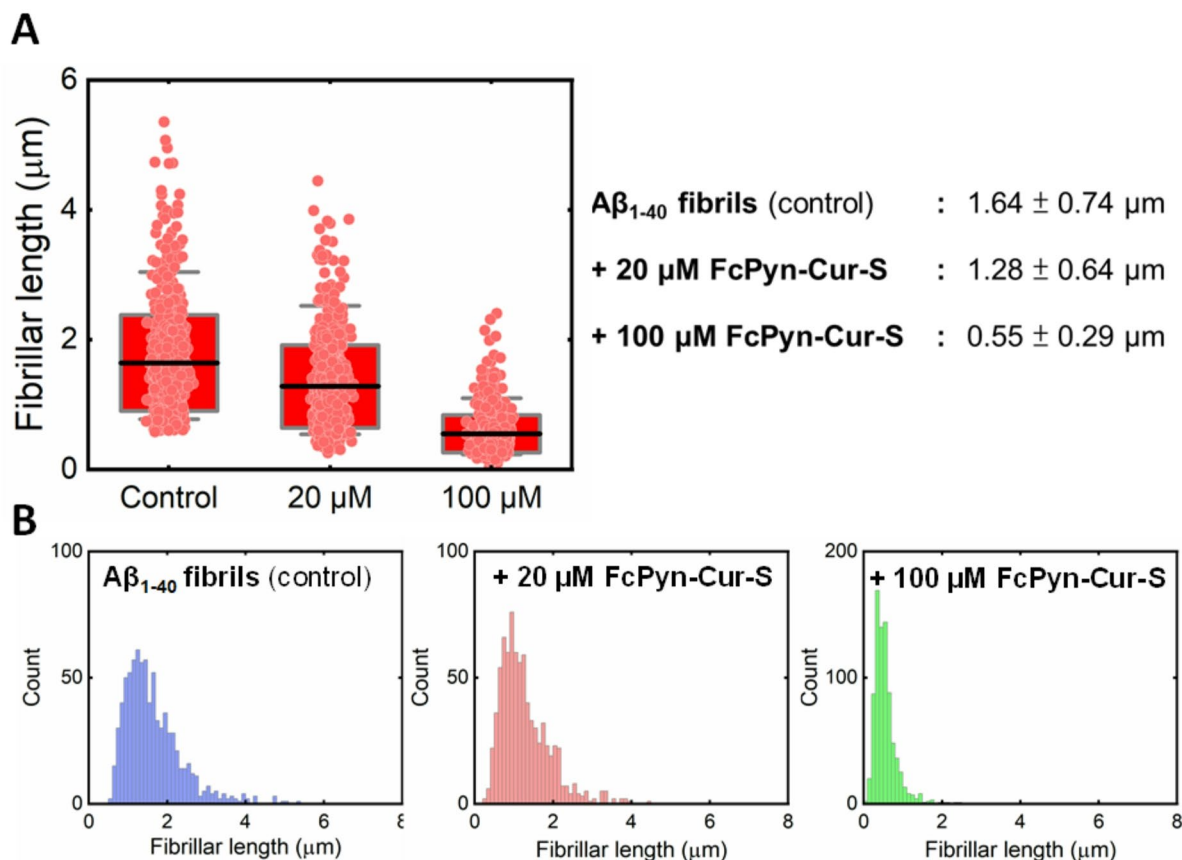


Fig. 6. SMLM Aβ₁₋₄₀ fibrils length determination after incubation with **FcPyn-Cur-S**. **A** - Aβ₁₋₄₀ fibrils length measurement. The black solid lines inside the box indicate the mean of the distribution. The box plots indicate the standard deviation of the distribution. The whiskers indicate 5–95% percentile of the distribution. **B** - The histogram for the measurement of the Aβ₁₋₄₀ fibrils incubated at different **FcPyn-Cur-S** concentrations.

Fragmentation of the Golgi apparatus, often associated with oxidative stress^{56,57} was not prominently observed. Although destabilised mitochondria (reduced mitochondrial potential, Figure S29) and morphological changes leading to cell death were noted in **FcPy-Cur-H** treated cells, the Golgi apparatus remained as a robust cluster rather than dispersed cisternae (see white arrows in Fig. 10). Similar Golgi clustering was observed in cells exposed to **FcPyn-Cur-O** and **FcPyn-Cur-S** curcumin derivatives. These findings suggest that mitochondrial signalling may play a more important role in the response of cells to **FcPy-Cur-H**, **FcPyn-Cur-O** and **FcPyn-Cur-S** treatments.

Western blot analysis of caspase-3 protein was performed to further investigate mitochondrial signalling of apoptosis. Protein bands of caspase-3 and GAPDH in whole-cell lysates are shown in Fig. 11. A substantial decrease in pro-caspase-3 protein levels (32 kDa) was observed in cells treated with **FcPyn-Cur-O** and **FcPyn-Cur-S**. This decrease likely reflects cleavage into active caspase-3 into shorter 15 kDa fragments, which are not detected under current experimental conditions, which may not be fully detected due to antibody specificity and size limitations. Therefore, while these results suggest mitochondrial involvement in apoptosis, they should be interpreted as indicative rather than definitive. These results support the hypothesis derived from the flow cytometry, that a mitochondrial signalling pathway leading to apoptosis is likely involved during treatment with **FcPyn-Cur-O** and **FcPyn-Cur-S**.

Conclusion

With the aim of improving the pharmacological properties of curcumin, four ferrocenyl pyrazole (**FcPy-Cur-H**, **FcPy-Cur-COPh**, **FcPy-Cur-COFc**, **FcPy-Cur-Me**) and two ferrocenyl pyrimidine (**FcPyn-Cur-O**, **FcPyn-Cur-S**) derivatives were synthesized via microwave irradiation and the Biginelli multicomponent reaction, respectively, and fully characterized by spectroscopic methods.

The *in vitro* experiments indicated a potential *dual-functional activity* of these compounds, which modulate Aβ fibrillogenesis in a concentration-dependent manner. All derivatives affected both the formation of Aβ amyloid fibrils and the disaggregation of preformed fibrils, with pyrimidine-based derivatives showing the most notable effects, suggesting a possible structure-activity relationship. Molecular docking analyses provided complementary insights, supporting the role of the ferrocene unit, aromatic moieties, and multiple hydrogen-

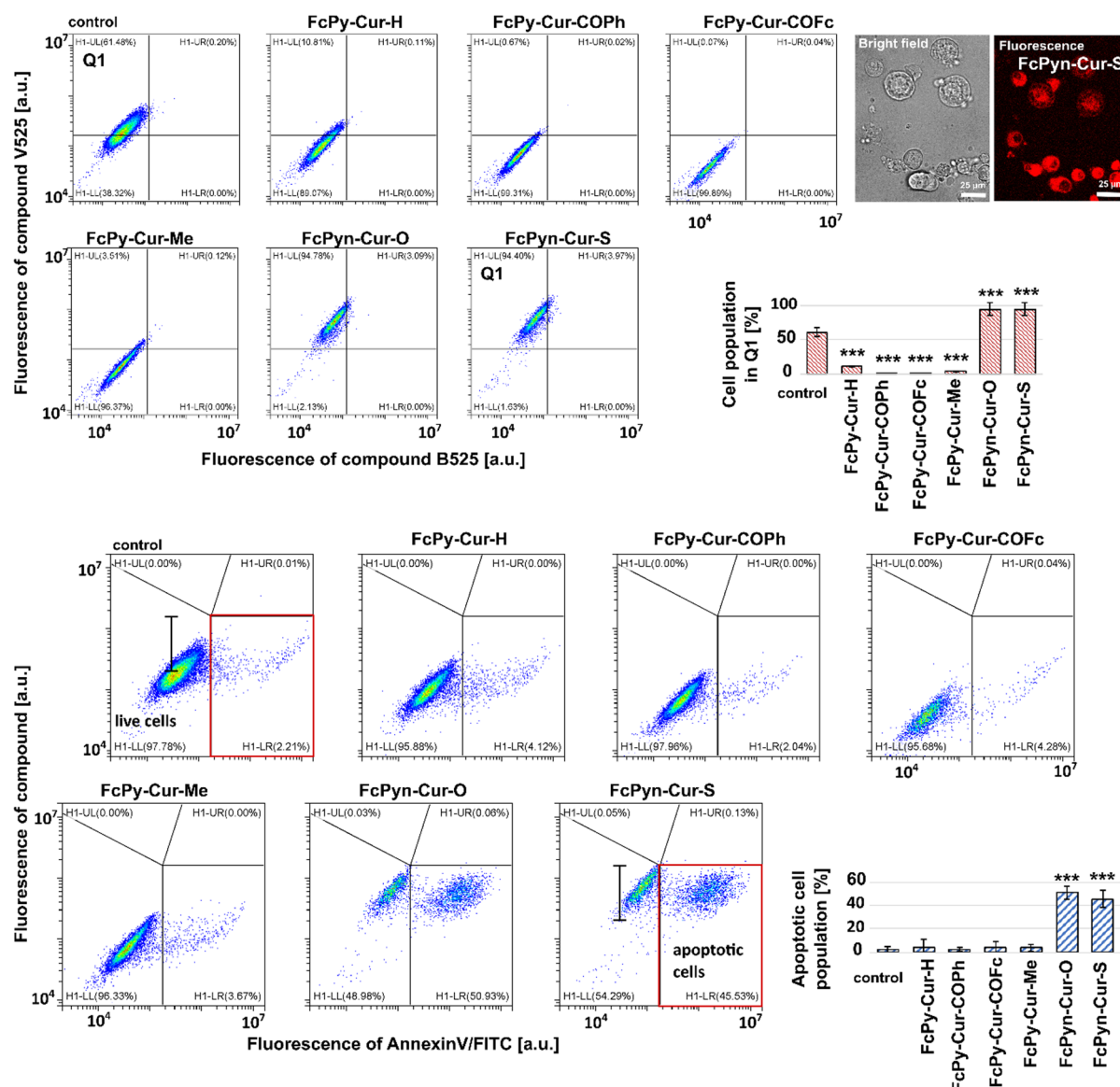


Fig. 7. (A) Flow cytometry analysis of 12.5 μ M ferrocene-containing analogues of curcumin uptake (24 h) by U87MG cells. Fluorescence was detected in two channels V525 and B525. The quantification of the Q1 quadrant is shown in histograms (lower right). A bright field and fluorescence image (the same excitation emission parameters as for V525) of cells exposed to 12.5 μ M **FcPyn-Cur-S** for 24 h are present in the upper right. The number of cells in correlation plots is colour-coded from blue to red. (B) Flow cytometry analysis of 12.5 μ M ferrocene-containing analogues of curcumin (24 h) effect on U87MG cells. Fluorescence AnnexinV/FITC was detected in channel B525 and autofluorescence of treated cells in V525. The red rectangles indicate the quadrant (lower right) related to apoptotic cells. The populations of cells in these quadrants were shown in histograms (lower right). A significant difference from the control was expressed with ***. The fluorescence of **FcPyn-Cur-O** and **FcPyn-Cur-S** in cells is indicated with a black marker. The number of cells in correlation plots is colour-coded from blue to red.

bond donors in the observed interactions, though the docking results should be interpreted as qualitative rather than quantitative predictors.

In addition, assessment of glioblastoma cell metabolic activity through MTT assay, Western blot, fluorescence microscopy, and flow cytometry suggested that the pyrimidine derivatives **FcPyn-Cur-O** and **FcPyn-Cur-S** exerted the most pronounced effects on cell proliferation, correlating with increased uptake, mitochondrial destabilization, and apoptosis induction.

Taken together, these findings point to dual anti-amyloidogenic and anticancer potential of ferrocene-containing curcumin derivatives, influenced by specific structural modifications. Nevertheless, the present study is limited to in vitro conditions, and no in vivo validation or pharmacokinetic analysis has yet been performed. Moreover, while docking provided a structural rationale for binding, it cannot fully capture the dynamic

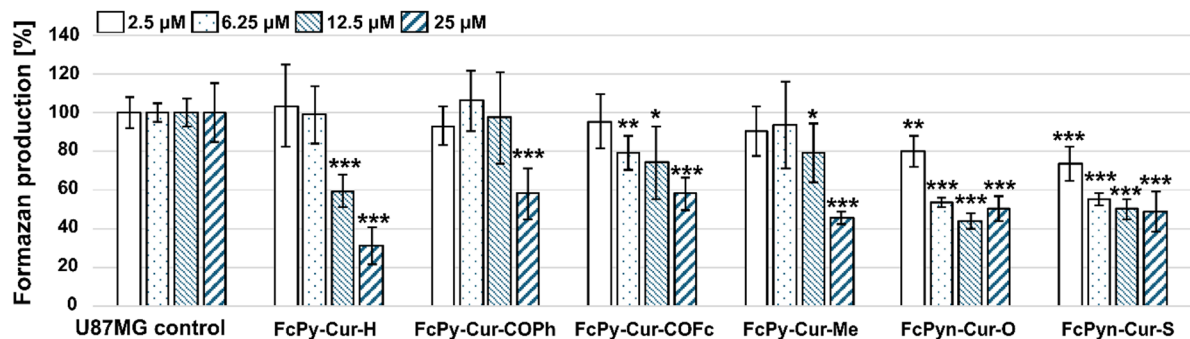


Fig. 8. MTT assay of ferrocene-containing analogues of curcumin biological activity in U87MG cells expressed as a percentage of formazan production. Cells were exposed to the curcumin derivatives for 48 h. Statistically significant differences between control and treatments were determined with a one-way ANOVA test: * $p < 0.05$, ** $p < 0.01$ and *** $p < 0.001$.

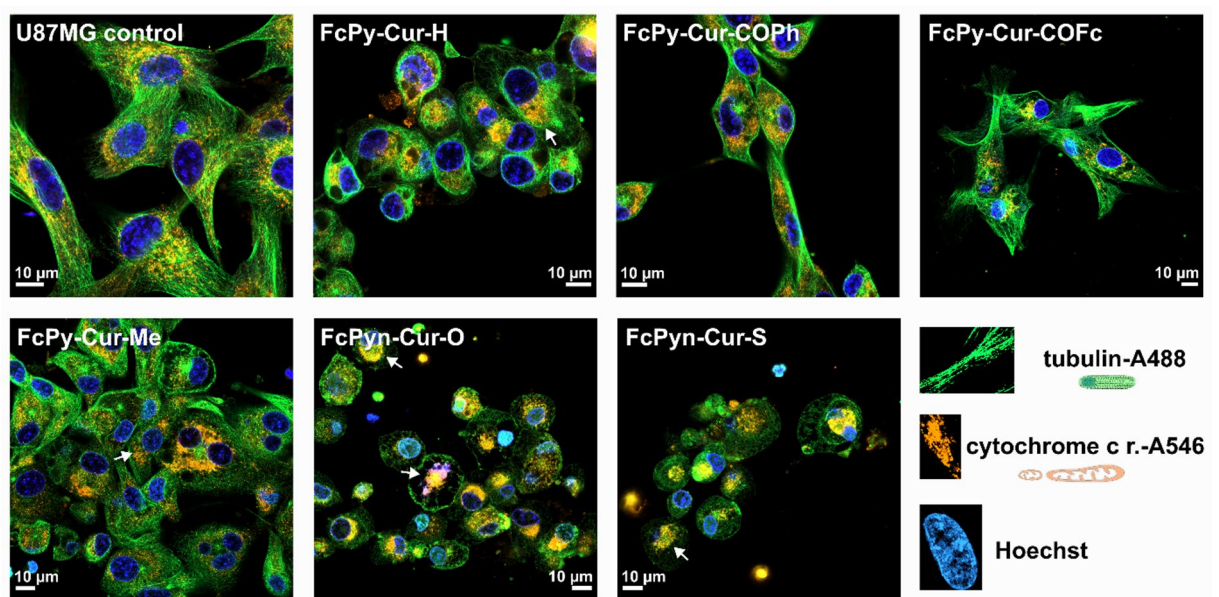


Fig. 9. Super-resolution fluorescence images of U87MG cells immuno-stained against α -tubulin excitation 488 nm, green fluorescence anti- α -tubulin conjugated with AlexaFluor 488, ab185031, 1:100), and ubiquinol-cytochrome *c* reductase (excitation 555 nm, orange fluorescence of anti- ubiquinol-cytochrome *c* reductase (ab110252, 1:100), secondary anti-mouse AlexaFluor 546 (ThermoFisher Scientific, 2:1000). Nuclei were counterstained with Hoechst 33342 (excitation 405 nm; blue fluorescence). Typical structures are shown in the lower right. Cells were exposed to 12.5 μ M of ferrocene-containing analogues of curcumin for 48 h. White arrows indicate the perinuclear localization of mitochondria.

aggregation process of A β peptides. Future studies should therefore aim to evaluate the stability, selectivity, and efficacy of these compounds in relevant animal models and further clarify their mechanisms of action.

All compounds significantly influenced both the formation of A β amyloid fibrils and the disaggregation of preformed fibrils, with the pyrimidine-based derivatives showing the most pronounced effects, highlighting a clear structure-activity relationship. Molecular docking analyses support these findings, indicating that the ferrocene unit, aromatic moieties, and multiple hydrogen-bond donors facilitate specific interactions with A β peptides and fibrillar aggregates.

Methods

General chemistry

The preparation of (*E*)-5-(4-hydroxy-3-methoxyphenyl)-1-ferrocenylpent-4-ene-1,3-dione (**A**) and (*E*)-5-(4-hydroxy-3-methoxyphenyl)-1-ferrocenyl-2-methylpent-4-ene-1,3-dione (**B**) was described in our previous work⁴³. Tetrahydrofuran (THF) used for the synthesis was refluxed under LiAlH₄, distilled and stored over molecular sieves (4 Å) under argon. Thin layer chromatography was performed on silica gel (Kieselgel 60

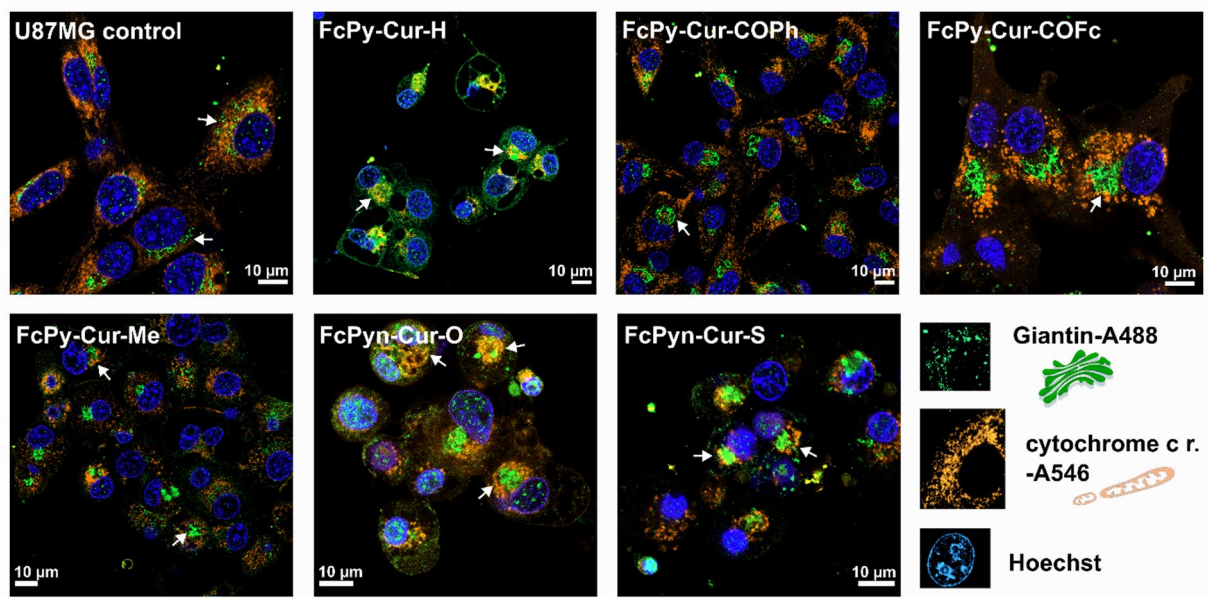


Fig. 10. Super-resolution fluorescence images of U87MG cells immunostained against Giantin (excitation 488 nm, green fluorescence of secondary antibody AlexaFluor 488, primary antibody anti-Giantin (ab80864, 1:100)) and ubiquinol-cytochrome *c* reductase (excitation 555 nm, orange fluorescence of anti-ubiquinol-cytochrome *c* reductase (ab110252, 1:100), secondary anti-mouse AlexaFluor 546 (ThermoFisher Scientific, 2:1000). Nuclei were counterstained with Hoechst 33342 (excitation 405 nm, blue fluorescence). Typical structures are shown in the lower right. Cells were exposed to 12.5 μ M of ferrocene-containing analogues of curcumin for 48 h. White arrows indicate the localization of the Golgi apparatus.

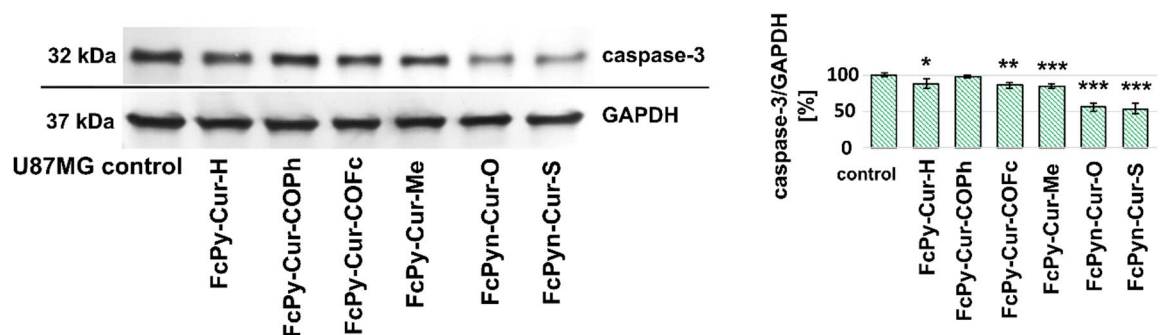


Fig. 11. Western blot analysis of caspase-3 (ab32351, 1:1000) and GAPDH in U87MG cells exposed to 12.5 μ M of ferrocene-containing analogues of curcumin for 48 h. Band densities were normalized to GAPDH and plotted in histograms (left). A significant difference was determined with a one-way ANOVA test: * $p < 0.05$, ** $p < 0.01$, *** $p < 0.001$. The experiment was performed in triplicates.

HF254, Merck) using petroleum ether/acetone or ethyl acetate/hexane mixture. The microwave-assisted reactions were carried out in microwave reactor Milestone (Start S). The melting points were determined using a Reichert Thermovar HT1 BT 11 melting point device. Infrared spectra were recorded as dichloromethane solutions of compounds in the wavelength range of 4000–600 cm^{-1} using a Spectrum Two FT-IR spectrometer (PerkinElmer) equipped with a deuterated triglycine sulphate (DTGS) detector. ^1H NMR spectra were recorded at 600.133 MHz and ^{13}C NMR spectra at 150.907 MHz using a Bruker Avance spectrometer. The chemical shifts (δ) are given in parts per million relative to tetramethylsilane as the internal standard and the coupling constants (J) in Hertz (Hz). Two-dimensional NMR experiments (COSY, HMBC, HSQC) were also performed to support the signal assignment. Mass spectra (ESI-MS) were recorded on an HPLC-MS system coupled with a triple-quadrupole mass spectrometer.

Synthesis of ferrocene-containing analogues

General procedure for the synthesis of ferrocene-containing pyrazole analogues of curcumin FcPy-Cur-H and FcPy-Cur-Me

Compound A or B (0.40 mmol) was dissolved in acetic acid (1 mL) in a round bottom flask and hydrazine monohydrate (0.90 mmol) was added. The reaction mixture was stirred for 20–40 min under reflux of the solvent in a microwave reactor at a temperature of 50 °C ($P=600$ W). When the chromatographic TLC plate showed the absence of the starting reactant, the reaction mixture was quenched by adding brine (5 mL) and worked up with dichloromethane. The organic layer was washed three times with brine, dried with anhydrous Na_2SO_4 and the solvent removed in vacuo. The crude product was purified by thin-layer chromatography on silica gel in petroleum ether/acetone mixture.

(E)-3(5)-[β -(4-hydroxy-3-methoxyphenyl)-ethenyl]-5(3)-ferrocenyl-1 H-pyrazole (**FcPy-Cur-H**)

Yellow solid (0.107 g, 67%); $R_f = 0.69$ in PE/acetone = 1/1; m.p. 101–103 °C; IR (CH_2Cl_2) $\nu_{\text{max}}/\text{cm}^{-1}$: 3533 w (OH)_{str}, 3446 w (NH)_{str}, 3054 w (=C-H)_{str}, 1515 m (NH)_{bend}, 1266 s (C-O). ^1H NMR (600 MHz, CDCl_3) δ/ppm : 8.58 (bs, 1H, NH), 7.03 (d, 1H, $^3J_{\text{H}8'} = 16.4$ Hz, H7'), 6.95 (d, 1H, $^3J_{\text{H}5'} = 7.6$ Hz, H6' Ph), 6.97 (s, 1H, H2' Ph), 6.93 (d, 1H, $^3J_{\text{H}7'} = 16.4$ Hz, H8'), 6.88 (d, 1H, $^3J_{\text{H}6'} = 8.0$ Hz, H5' Ph), 6.56 (s, 1H, H4), 5.29 (s, 1H, OH), 4.71 (bs, 2 H, Fc), 4.30 (bs, 2 H, Fc), 4.06 (s, 5 H Fc), 3.83 (s, 3 H, OCH_3). ^{13}C NMR APT (150 MHz, CDCl_3) δ/ppm : 146.38 (C3, C5), 145.43 (C3', C4'), 130.08 (C7'), 128.89 (C1'), 120.08 (C6'), 115.78 (C5'), 114.23 (C8') 107.72 (C2'), 99.02 (C4), 75.11 (C1, Fc), 69.16 (5 C, Fc), 68.36, 66.05 (2 \times 2 C, Fc), 55.34 (OCH_3). ESI-MS for $\text{C}_{22}\text{H}_{20}\text{FeN}_2\text{O}_2$: calculated $m/z = 400.25$, found 401.10 [(M+H)⁺].

(E)-3(5)-[β -(4-hydroxy-3-methoxyphenyl)-ethenyl]-5(3)-ferrocenyl-4-methyl-1 H-pyrazole (**FcPy-Cur-Me**)

Yellow solid (0.108 g, 65%); $R_f = 0.61$ in PE/acetone = 2/1; m.p. 113–115 °C. IR (CHCl_3) $\nu_{\text{max}}/\text{cm}^{-1}$: 3537 m (OH)_{str}, 3448 m (NH)_{str}, 1516 s (NH)_{bend}, 1269 s (C-O). ^1H NMR (600 MHz, DMSO- d_6) δ/ppm : 12.50 (bs, 1H, NH), 9.11 (s, 1H, OH), 7.18 (bs, 1H, H2' Ph), 7.03 (d, 1H, $^3J_{\text{H}8'} = 16.5$ Hz, H7'), 6.96–6.93 (m, 2H, H6' Ph, H8'), 6.77 (d, 1H, $^3J_{\text{H}7'} = 8.1$ Hz, H5' Ph), 4.68 (bs, 2 H, Fc), 4.31 (bs, 2 H, Fc), 4.09 (s, 5 H, Fc), 3.84 (s, 3 H, OMe), 2.29 (s, 3 H, Me). ^{13}C NMR APT (150 MHz, DMSO- d_6) δ/ppm : 147.86 (C3, C5, C3', C4'), 146.60 (C4) 128.41 (C6'), 128.10 (C1'), 119.94 (C7'), 115.56 (C5', C8'), 109.59 (C2'), 68.93 (5 C, Fc), 68.00, 66.29 (2 \times 2 C, Fc), 67.37 (C1, Fc), 55.64 (OMe), 9.10 (Me). ESI-MS for $\text{C}_{23}\text{H}_{22}\text{FeN}_2\text{O}_2$: calculated $m/z = 414.27$, found 415.15 [(M+H)⁺].

General procedure for the synthesis of ferrocene-containing pyrazole analogues of Curcumin FcPy-Cur-COPh and FcPy-Cur-COFc

To a dichloroethane solution (1.5 mL) of compound **FcPy-Cur-H** (0.43 mmol) was added acyl chloride (PhCOCl or FcCOCl) (0.69 mmol). The reaction mixture was stirred under reflux in a microwave reactor at a temperature of 90 °C ($P=1000$ W). The reaction was stopped after 30 min (for the preparation of **FcPy-Cur-COPh**) or 45 min (for the preparation of **FcPy-Cur-COFc**) when the chromatographic TLC plate showed the absence of the starting reactant, and the reaction mixture was worked up with dichloromethane. The organic layer was washed three times with brine, dried with anhydrous Na_2SO_4 and the solvent was removed in vacuo. The crude product was purified by thin-layer chromatography on silica gel in petroleum ether/acetone = 3/1.

(E)-3(5)-[β -(4-hydroxy-3-methoxyphenyl)-ethenyl]-5(3)-ferrocenyl-1 H-pyrazole-1-yl-(phenyl) methanone (**FcPy-Cur-COPh**)

Orange solid (0.150 g, 69%); $R_f = 0.71$ in PE/acetone = 2/1; m.p. 77–79 °C. IR (CH_2Cl_2) $\nu_{\text{max}}/\text{cm}^{-1}$: 3531 w (OH)_{str}, 3057 w (=C-H)_{str}, 1697 m (C=O)_{str}, 1269 s (C-O). ^1H NMR (600 MHz, CDCl_3) δ/ppm : 8.07 (d, 2H, H2'' H6'', Ph-C=O), 7.72 (d, 1H, $^3J_{\text{H}7''} = 16.3$ Hz, H8''), 7.60 (t, 1H, H4'', Ph-C=O), 7.49 (t, 2H, H3'' H5'', Ph-C=O), 7.14 (d, 1H, $^3J_{\text{H}8'} = 16.3$ Hz, H7'), 7.10 (bs, 1H, H2' Ph), 7.06 (dd, 1H, $^3J_{\text{H}5'} = 8.1$ Hz, H6' Ph), 6.92 (d, 1H, $^3J_{\text{H}6'} = 8.1$ Hz, H5' Ph), 6.77 (s, 1H, H4), 5.88 (bs, 1H, OH), 4.72 (bs, 2H, H2 H5, Fc), 4.33 (bs, 2H, H3 H4, Fc), 4.12 (s, 5H, Fc), 3.94 (s, 3H, OCH_3). ^{13}C NMR APT (150 MHz, CDCl_3) δ/ppm : 168.28 (C=O), 153.79 (C5), 146.41 (C3'), 146.34 (C3), 145.95 (C4'), 133.11 (C7'), 132.87 (C1'', Ph-C=O), 132.16 (C4'', Ph-C=O), 131.27 (2 C, C3'' C-5'', Ph-C=O), 128.62 (C1'), 127.32 (2 C, C2'' C6'', Ph-C=O), 121.22 (C6'), 114.33 (C5'), 114.09 (C8'), 107.65 (C2'), 104.31 (C4) 75.77 (C1, Fc), 69.09 (5 C, Fc), 68.86 (2 C, Fc), 66.81 (2 C, Fc), 55.49 (OCH_3). ESI-MS for $\text{C}_{29}\text{H}_{24}\text{FeN}_2\text{O}_3$: calculated $m/z = 504.35$, found 505.10 [(M+H)⁺].

(E)-3(5)-[β -(4-hydroxy-3-methoxyphenyl)-ethenyl]-5(3)-ferrocenyl-1 H-pyrazole-1-yl-(ferrocenyl) methanone (**FcPy-Cur-COFc**)

Orange solid (0.137 g, 52%); $R_f = 0.56$ in PE/acetone = 3/1; m.p. 100–101 °C. IR (CH_2Cl_2) $\nu_{\text{max}}/\text{cm}^{-1}$: 3534 w (OH)_{str}, 3057 w (=C-H)_{str}, 1678 m (C=O)_{str}, 1269 s (C-O). ^1H NMR (600 MHz, CDCl_3) δ/ppm : 7.80 (d, 1H, $^3J_{\text{H}8'} = 16.3$ Hz, H7'), 7.11–7.03 (m, 3H, H2', H8', H6'), 6.93 (d, 1H, $^3J_{\text{H}5'} = 8.1$ Hz, H5' Ph), 6.70 (s, 1H, H4), 5.45 (bs, 2 H, Fc-C=O), 4.84 (bs, 2 H, Fc-pyr.), 4.62 (bs, 2 H, Fc-C=O), 4.39 (bs, 2 H, Fc-pyr.), 4.26 (bs, 5 H, Fc-C=O), 4.14 (bs, 5 H, Fc-pyr.), 3.97 (s, 3 H, OCH_3). ^{13}C NMR APT (150 MHz, CDCl_3) δ/ppm : 171.75 (C=O), 152.75 (C5), 146.30 (C3'), 145.88 (C3), 145.81 (C4'), 132.75 (C7'), 128.83 (C1'), 121.07 (C6'), 115.02 (C5'), 114.106 (C8'), 107.83 (C2'), 103.52 (C4), 76.23 (C_{quat} , Fc-C=O), 73.15 (2 C, Fc-C=O), 72.63 (C_{quat} , Fc-pyr.), 72.10 (2 C, Fc-C=O), 69.78 (5 C, Fc-C=O), 69.10 (5 C, Fc-pyr.), 68.90 (2 C, Fc-pyr.), 66.61 (2 C, Fc-pyr.), 55.55 (OCH_3). ESI-MS for $\text{C}_{33}\text{H}_{28}\text{Fe}_2\text{N}_2\text{O}_3$: calculated $m/z = 612.28$, found 613.05 [(M+H)⁺].

General procedure for the synthesis of ferrocene-containing pyrimidine derivatives of curcumin FcPyn-Cur-O and FcPyn-Cur-S

Ferrocene carboxaldehyde (1 mmol), powdered urea or thiourea (1.2 mmol) and a catalytic amount of piperidine (0.001 mmol) were added to a warm solution of curcumin (1 mmol) in dry tetrahydrofuran (3 mL). The mixture

was stirred and heated at a temperature of 80 °C and the conversion of the reactant to the product was monitored by thin layer chromatography in a mixture of EtOAc/hexane = 1/1. Despite the low presence of reactants on the TLC plate, the reaction was stopped after 48 h as a darkening of the solution with the appearance of insoluble dark particles was observed. The reaction mixture was filtered and worked up with 60 ml ethyl acetate. The organic layer was washed three times with brine, dried with anhydrous Na₂SO₄ and the solvent removed in vacuo. The crude product was purified by thin-layer chromatography on silica gel in the EtOAc/hexane mixture.

5-[3-(4-Hydroxy-3-methoxyphenyl)-1-oxoprop-2-en-1-yl]-6-[2-(4-hydroxy-3-methoxyphenyl) ethen-1-yl]-4-ferrocenyl-3,4-dihydropyrimidine-2(1 H)-one (FcPyn-Cur-O)

Dark red solid (0.175 g, 29%); R_f = 0.40 in EtOAc/hexane = 1/1; m.p. >350 °C. IR (CH₂Cl₂) ν_{\max} /cm⁻¹: 3527 m (OH)_{str}, and (NH)_{str}, 3014 w (=C-H)_{str}, 2978 w, 2941 w (C-H)_{str}, 1638 m, 1595 s (C=O)_{str}, 1513 s (NH)_{bend}, 1269 s (C-O)_{str}. ¹H NMR (600 MHz, CDCl₃) and ¹³C NMR APT (150 MHz, CDCl₃) are listed in Table 1. ESI-MS for C₃₃H₃₀FeN₂O₆: calculated m/z = 606, found 641 [M + Cl]⁻.

5-[3-(4-Hydroxy-3-methoxyphenyl)-1-oxoprop-2-en-1-yl]-6-[2-(4-hydroxy-3-methoxyphenyl) ethen-1-yl]-4-ferrocenyl-3,4-dihydropyrimidine-2(1 H)-thioetone (FcPyn-Cur-S)

Dark red solid (0.155 g, 25%); R_f = 0.39 in EtOAc/hexane = 1.2/1; m.p. >350 °C. IR (CH₂Cl₂) ν_{\max} /cm⁻¹: 3527 w (OH)_{str}, 3406 vw (NH)_{str}, 3057 w (=C-H)_{str}, 2974 w, 2945 w (C-H)_{str}, 1595 m (C=O)_{str}, 1513 m (NH)_{bend}, 1269 s (C-O)_{str}. ¹H NMR (600 MHz, CDCl₃) and ¹³C NMR APT (150 MHz, CDCl₃) are listed in Table 1. ESI-MS for C₃₃H₃₀FeN₂O₅S: calculated m/z = 622, found 655 [M + CH₃OH + H]⁺.

Molecular docking study

The molecular binding calculations were performed using AutoDock software specifically employing the Lamarckian Genetic algorithm^{58,59}. Protein crystal structures were obtained from the online “Protein Data Bank (PDB)” and directly imported into AutoDock for analysis. For the protein, PDB ID: 2LMN was used⁶⁰. Ligands were designed using ChemOffice and Gaussview, and their energies were minimized using PM6^{61,62} semi-empirical method through Gaussian Software⁶³.

Examination of anti-amyloid activity of ferrocene-containing analogues

Amyloid β (1–40) fibrillization

Amyloid beta peptide (1–40) (A β _{1–40}) was purchased from rPeptide (Cat # A-1001-2, Lot# 10290940T). A stock solution of A β _{1–40} (~ 450 μ M) was prepared by dissolving the lyophilized peptide in 10 mM NaOH, then-after sonicated for 1 min in a water bath sonicator, followed by centrifugation for 10 min (12 000 g) at 4 °C to precipitate large aggregates. The concentration was determined spectrophotometrically using ϵ_{280} = 1490 M⁻¹cm⁻¹. For fibrillization, A β _{1–40} stock solution was further diluted to 25 μ M in 150 mM MOPS buffer containing 0.035% of Na₃, pH 6.9 (hereinafter referred to as MOPS buffer, pH 6.9) and incubated for up to 7 days at 37 °C^{33,42,43,53}.

Estimation of ferrocene-containing analogues of curcumin anti-amyloidogenic activity by thioflavin T fluorescence assay

The protein amyloid fibrillation and anti-amyloidogenic efficacy of ferrocene-conjugated curcumin analogues were assessed using a Thioflavin T (ThT) fluorescence assay. Fluorescence measurements were conducted in black 96-well microplates employing a Synergy MX spectrofluorometer (BioTek Instruments). The ThT probe was excited at 440 nm, and emission was monitored at 485 nm. Both excitation and emission slit widths were set to 9.0 nm, and the vertical offset for the top-read optical probe was maintained at 6 nm^{45,54,64,65}.

For the concentration-dependent analysis, previously described procedure has been followed:^{45,54,64} briefly, each of 6 ferrocene-containing analogues of curcumin freshly dissolved in dimethyl sulfoxide (DMSO), was added to 25 μ M of A β _{1–40} in MOPS buffer (150 mM, pH 6.9) yielding final compound concentrations ranging from 0.05 μ M to 1 mM. The mixtures were incubated at 37 °C for 7 days to promote fibril formation. Subsequently, ThT was added to each sample at a final molar ratio of peptide to dye of 1:5. Samples were incubated for an additional hour at 37 °C before fluorescence was recorded. The fibril-disassembling activity of the curcumin analogues was evaluated by incubating preformed A β _{1–40} fibrils (25 μ M) with the test compounds at concentrations spanning 0.05 μ M to 1 mM at 37 °C for 24 h. Following incubation, ThT was added as described above, and samples were allowed to equilibrate for 1 h at 37 °C prior to fluorescence analysis^{45,54,64,65}.

Inhibitory concentration 50% (IC₅₀) values, indicative of compound potency in preventing amyloid fibrillogenesis, and disaggregation concentration 50% (DC₅₀) values, reflective of the ability to disrupt preformed fibrils, were derived from fluorescence intensity measurements. Relative fibril content was inferred from ThT fluorescence, with signal intensities normalized to the control sample comprising aggregated A β _{1–40} in the absence of test compounds (defined as 100% fibrillation). All experimental conditions were replicated independently five times. Data are reported as mean \pm standard deviation (SD) based on five technical replicates^{45,54,64,65}.

The obtained dose-dependent data were fitted by four-parameter sigmoidal logistic equation of the form:

$$Y = A_2 + \frac{A_2 - A_1}{1 + \left(\frac{x}{x_{50}}\right)^b}$$

where Y is the observed fluorescence intensity, A_1 and A_2 represent the maximal and minimal fluorescence values, respectively, x is the concentration of the test compound, x_{50} denotes the concentration corresponding to 50% inhibition (IC₅₀ or DC₅₀), and b is the Hill slope, indicating the steepness of the curve. Nonlinear regression

and all associated calculations were performed using SigmaPlot software version 14.5 (Systat Software, Inc.) as described previously^{45,54,64}.

Atomic force microscopy visualization

Atomic force microscopy (AFM) was utilized to characterize the morphological features of A β ₁₋₄₀ fibrils alone and in the presence of ferrocene analogues of curcumin. For sample preparation, 10 μ L aliquots of each solution were carefully dispensed onto freshly cleaved mica discs of the highest grade (V1, Ted Pella, Inc., Redding, CA, USA). The adsorption process was allowed to proceed for 5–10 min at 25 ± 1 °C. Subsequently, the mica surfaces were gently rinsed with ultrapure water (18.2 M Ω -cm) to remove unbound material, and the samples were dried under a controlled stream of purified nitrogen. AFM imaging was conducted using a Veeco di Innova Scanning Probe Microscope (Bruker AXS Inc., Madison, WI, USA) operating in tapping mode. AFM scans were acquired using an antimony (n)-doped silicon cantilever (NCHV, Bruker AXS Inc.) with a nominal spring constant of 42 N/m and a resonance frequency of approximately 320 kHz. Scanning was carried out at a rate of 0.5–0.75 kHz. Images were captured at 1024 \times 1024 pixels per frame. Raw AFM data were processed and analyzed using NanoScope Analysis software, version 1.20 (Bruker AXS Inc., Madison, WI, USA). No post-processing procedures such as image smoothing or noise reduction were applied to preserve the integrity of the raw morphological data^{33,42,52}.

Single-molecule localization microscopy

The single-molecule localization microscopy (SMLM) was used to evaluate the morphology of A β fibrils in the absence/presence of **FcPyn-Cur-S** treatment. The amyloid-beta fibrils and **FcPyn-Cur-S** were diluted to the concentrations of 20 μ M and 1 mM using 1 \times PBS solution. Subsequently, **FcPyn-Cur-S** was added into the 20 μ M A β fibril solution to obtain the final concentration of **FcPyn-Cur-S** in A β fibril solution to be 20 and 100 μ M. Moreover, a 20 μ M A β fibril solution without the addition of **FcPyn-Cur-S** was also used as a reference. After vortexing three times with each 30 s, three solutions were incubated for 1 h at room temperature. The glass coverslips were soaked in a 5% hydrochloric acid solution and sonicated for 0.5 h in the sonicating water bath. After rinsing with the deionized (DI) water, the glass coverslips were further sonicated in ethanol and DI water for 0.5 h to complete the cleaning process. The three A β fibril solutions were deposited on the well-cleaned glass coverslips and dried at room temperature. Based on the previously reported SMLM imaging approach, a 1 \times PBS solution containing 100 nM Nile red fluorophores were adopted as the imaging buffer. The excitation light used in the SMLM imaging was a 561 nm solid-state laser with an excitation power of 17 mW. The excitation light was enlarged by its beam size using a beam expander and then went to a custom-built wide-field fluorescence microscope equipped with a 1.49-NA oil immersion objective lens (100 \times UAPON100XOTIRF, Olympus). The objective lens collected the blinking fluorescence signals of Nile red fluorophores transiently attached to A β fibrils. After passing a dichroic beamsplitter (FF562-Di03, Semrock) and an emission filter (ET670/50, Chroma), the fluorescence images were obtained by an imaging lens and an electron-multiplying charge-coupled device (EMCCD) camera (iXon Ultra 897, Andor). The pixel size of the fluorescence image was approximately 93 nm \times 93 nm and the exposure time was set to 30 ms. 8000 fluorescence images were recorded to reconstruct an SMLM image by the ThunderSTORM plugin of ImageJ.

Anticancer activity of ferrocene-containing analogues of curcumin

Human glioblastoma cells of line U87MG (purchased from Cells Lines Services, Eppelheim, Germany) were propagated in 5% CO₂, 37 °C and humidified atmosphere according to cultivation protocol. Cells were grown in medium Dulbecco's modified Eagle medium (D-MEM, high glucose, GlutaMAX[™], with pyruvate, Gibco-Invitrogen, Life Technologies Ltd., Paisley, UK) and 10% fetal bovine serum (biosera, Nuaille, France), supplemented with penicillin/streptomycin (Gibco-Invitrogen, Life Technologies Ltd., Paisley, UK). One day before the experiment, the cell cultures were seeded in 96-well plates (SPL, Pocheon-si, Republic of Korea), Petri dishes (SPL) and 8-well plates for confocal fluorescence microscopy (ibidi, Grafelfing, Germany). Cells were treated with 2.5–25 μ M ferrocene-containing analogues of curcumin for 24 and 48 h according to the experimental protocol. The total amount of DMSO was not more than 1%.

Flow cytometry was used to assess the uptake of the curcumin derivatives by the U87MG cells and to identify apoptotic cell populations. Cell cultures were treated with 12.5 μ M of the ferrocene-containing analogues of curcumin for 24 h. Prior to detection, treated cells were detached with trypsin/ethylenediaminetetraacetic acid (ThermoFisher Scientific, Waltham, MA, USA), centrifuged and resuspended in 0.5 mL of 4°C cold PBS. To study the apoptotic response of U87MG cells, cultures in suspension were stained for 15 min with AnnexinV/FITC (Mitenyi Bi-otec B.V. & Co. KG, Bergisch Gladbach, Germany) according to the supplier's protocol. The cell suspensions were measured with the CytoFlex S analyser (Beckman Coulter, CA, USA) in channels V525 (fluorescence of curcumin derivatives) and B525 (autofluorescence and AnnexinV/FITC fluorescence). A constant volume of 30 μ L was measured and 2×10^4 cells were analysed.

Confocal vital fluorescence microscopy was performed with an LSM 700 ZEISS inverted microscope (ZEISS, Oberkochen, Germany), a 40x water immersion objective and laser excitation of 405 nm. The emission was filtered above 490 nm.

Immunofluorescence was used to identify subcellular changes related to mitochondria, Golgi apparatus and α -tubulin. U87MG cells were treated with 12.5 μ M ferrocene-containing analogues of curcumin for 48 h. After treatment, cells were fixed with 4% paraformaldehyde (Centralchem, Bratislava, Slovakia) for 7 min at room temperature and washed three times with cold PBS. The cells were penetrated with a (1:1) solution of methanol/acetone (Centralchem, Bratislava, Slovakia) for 4 min at -20 °C. The cells were washed again three times and blocked for 1 h at room temperature in 5% bovine serum albumin (BSA, Sigma Aldrich, Germany) and skimmed milk. Cells were washed and incubated overnight at 4 °C with primary antibodies (abcam, Cambridge, UK):

anti- α -tubulin conjugated with AlexaFluor 488 (ab185031), anti-ubiquinol-cytochrome *c* reductase (ab110252, mouse) and anti-Giantin (ab80864, rabbit) in 2.5% BSA solution (1:100). Cells were washed after incubation and exposed to secondary antibodies: anti-rabbit AlexaFluor 488 (abcam) and anti-mouse AlexaFluor 546 (ThermoFisher Scientific, Waltham, MA). The cells were washed three times. One wash step was supplemented by staining with Hoechst 33342 (ThermoFisher Scientific). Finally, the cells were mounted with Fluoroshield™ mounting medium (Sigma-Aldrich, USA).

The fluorescence images of the immunoassayed cells were captured using the LSM 900 microscope with Airyscan 2 detector (ZEISS) for multiplex super-resolution and higher sensitivity when scanning the samples. The Plan-Apochromat 63x/1.4 Oil DIC M27 objective (ZEISS) was used to acquire the images in super-resolution mode. The Joint Deconvolution (ZEISS) plugin was used for post-processing. Three laser sources were used to excite the samples: 405 nm for Hoechst detection (400–505 nm emission detection), 488 nm for AlexaFluor 488 (450–545 nm emission detection) and 561 nm for AlexaFluor 546 (450–700 nm) detection. The images were analysed using ZEISS ZEN 3.10 software.

Western blot analysis was performed to determine the changes in caspase-3 protein levels. Cells were exposed to 12.5 μ M ferrocene-containing analogues of curcumin for 48 h. The cell lysate was extracted from the cells by cell lysis with a radioimmunoprecipitation buffer (RIPA: 150 mM sodium chloride, 1% Triton X-100, 0.5% sodium deoxycholate, 0.1% sodium dodecyl sulphate, 50 mM Tris at pH 8; chemicals were purchased from Sigma-Aldrich). An inhibitor cocktail (Halt™ Protease and Phosphatase Inhibitor Cocktail, ThermoFisher Scientific) was used to inhibit phosphatases and proteases. Proteins were diluted in Laemmli buffer (Sigma Aldrich) before electrophoresis was performed in 12% polyacrylamide gels (10 μ l of sample per well). The proteins were transferred to a nitrocellulose membrane (porosity of 0.22 μ m; AppliChem; Darmstadt, Germany). The membranes were blocked for 1 h at room temperature in 5% skimmed milk/BSA and incubated overnight with primary antibodies: anti-caspase-3 (ab32351, abcam) and anti-GAPDH (glyceraldehyde 3-phosphate dehydrogenase, ab181602, abcam) at 4 °C. The membranes were washed and exposed to secondary antibodies for 1 h at room temperature. They were then stained with a chromogenic substrate from the Western Breeze Chromogenic Kit (ThermoFisher Scientific) according to the supplier's protocol. Protein bands were analyzed, and statistical analysis was performed using the Student t-test: * $p < 0.05$, ** $p < 0.01$, and *** $p < 0.001$.

The viability of cells exposed to ferrocene-containing analogues of curcumin for 48 h was investigated using 3-(4,5-dimethylthiazol-2-yl)-2,5-diphenyltetrazolium bromide (MTT, Sigma-Aldrich) solution. In this assay, the mitochondria of cells produce purple formazan that is related to their metabolic activity and reflects viability of the cells (the more formazan, the higher the viability of the cells). Cells were treated in 96-well plates with 2.5, 6.25, 12.5 and 25 μ M ferrocene-containing analogues of curcumin for 48 h. The next, MTT reagent was then added to the cell culture medium for 1 h according to the supplier's protocol. After incubation, the medium was removed and the formazan crystals were dissolved in 100% DMSO solution. The absorbance was measured at 560 nm using a plate reader. The background at 700 nm was subtracted from the absorbance of the formazan. The average values of 6 measurements were calculated and the percentage of formazan production was determined in comparison on the untreated control. Statistical analysis was performed using the one-way ANOVA test: * $p < 0.05$, ** $p < 0.01$, and *** $p < 0.001$. The experiment was repeated in triplicate.

Data availability

All data generated or analyzed during this study are included in this published article and its supplementary information files. Additional datasets that support the findings of this study are available from the corresponding author upon reasonable request.

Received: 10 July 2025; Accepted: 7 October 2025

Published online: 13 November 2025

References

- Khan, S. S., Singer, B. D. & Vaughan, D. E. Molecular and physiological manifestations and measurement of aging in humans. *Aging Cell*. **16** (4), 624–633 (2017).
- Nichols, E., Steinmetz, J. D. & Vollset, S. E. Estimation of the global prevalence of dementia in 2019 and forecasted prevalence in 2050: an analysis for the global burden of disease study 2019. *Lancet Public Health*. **7** (2), 105–125 (2022).
- Selkoe, D. J. & Lansbury, P. J. *Alzheimer's Disease Is the Most Common Neurodegenerative Disorder. Basic Neurochemistry: Molecular, Cellular and Medical Aspects*. 6th Ed. (Lippincott-Raven, 1999).
- Hake, G., Mhaske, A. & Shukla, R. Drug delivery strategies in Alzheimer's disease. In *Drug Delivery Strategies in Neurological Disorders: Challenges and Opportunities*. (Eds. Mishra, A. & Kulhari, H.) (Springer, 2023).
- Long, S., Benoist, C. & Weidner, W. *World Alzheimer Report 2023: Reducing Dementia Risk: Never Too early, Never Too Late* (Alzheimer's Disease International, 2023).
- Tanzi, R. E. & Bertram, L. Twenty years of the Alzheimer's disease amyloid hypothesis: a genetic perspective. *Cell* **120**, 545–555 (2005).
- Bloom, G. S. Amyloid- β and tau: the trigger and bullet in Alzheimer disease pathogenesis. *JAMA Neurol*. **71** (4), 505–508 (2014).
- d'Errico, P. & Meyer-Luehmann, M. Mechanisms of pathogenic Tau and A β protein spreading in Alzheimer's disease. *Front. Aging Neurosci.* **12**, 265 (2020).
- Zhang, H. et al. Interaction between A β and Tau in the pathogenesis of Alzheimer's disease. *J. Biol. Sci.* **17**, 2181–2192 (2021).
- Hardy, J. & Allsop, D. Amyloid deposition as the central event in the aetiology of Alzheimer's disease. *Trends Pharmacol. Sci.* **12**, 383–388 (1991).
- Hardy, J. & Higgins, G. Alzheimer's disease: the amyloid cascade hypothesis. *Science* **256**, 184–185 (1992).
- Spies-Jones, T. L. et al. Tau pathophysiology in neurodegeneration: a tangled issue. *Trends Neurosci.* **32** (3), 150–159 (2009).
- Abdelnour, C. et al. Perspectives and challenges in patient stratification in Alzheimer's disease. *Alzheimers Res. Ther.* **14**, 112 (2022).
- Ratan, Y. et al. An insight into cellular and molecular mechanisms underlying the pathogenesis of neurodegeneration in Alzheimer's disease. *Biomedicine* **11**, 1398 (2023).

15. Kamatham, P. T. et al. Pathogenesis, diagnostics, and therapeutics for Alzheimer's disease: breaking the memory barrier. *Ageing Res. Rev.* **101**, 102481 (2024).
16. Zhang, J. et al. Recent advances in Alzheimer's disease: mechanisms, clinical trials and new drug development strategies. *Sig Transduct. Target. Ther.* **9**, 211 (2024).
17. Jovčevska, I. et al. Glioma and glioblastoma - how much do we (not) know? *Mol. Clin. Oncol.* **1**, 935–941 (2013).
18. Pradeep, S. et al. Exploring shared therapeutic targets for Alzheimer's disease and glioblastoma using network Pharmacology and protein-protein interaction approach. *Front. Chem.* **13**, 1549186 (2025).
19. Ainslie, A. P. et al. Glioblastoma is associated with extensive accelerated brain ageing. *Ageing Cell.* **23** (3), e14066 (2024).
20. Shi, J. & Huang, S. Comparative insight into microglia/macrophages-associated pathways in glioblastoma and Alzheimer's disease. *Int. J. Mol. Sci.* **25**, 16 (2024).
21. Liu, T. et al. Potential role of TNFRSF12A in linking glioblastoma and Alzheimer's disease via shared tumour suppressor pathways. *Sci. Rep.* **15**, 21535 (2025).
22. Sánchez-Valle, J. et al. A molecular hypothesis to explain direct and inverse co-morbidities between Alzheimer's disease, glioblastoma and lung cancer. *Sci. Rep.* **7**, 4474 (2017).
23. Greutter, L. et al. Frequent Alzheimer's disease neuropathological change in patients with glioblastoma. *Neuro-Oncology Adv.* **6** (1), vdae118 (2024).
24. Liang, G. et al. Synthesis, crystal structure and anti-inflammatory properties of curcumin analogues. *Eur. J. Med. Chem.* **44** (2), 915–919 (2009).
25. Oglah, M. K. et al. Curcumin and its derivatives: A review of their biological activities. *Sys Rev. Pharm.* **11** (3), 472–481 (2020).
26. Cklamunt, R. M. et al. Curcumin derived pyrazoles and related compounds. *Afinidad* **576**, 259–268 (2016).
27. Ahmed, M. et al. Screening of curcumin-derived isoxazole, pyrazoles, and pyrimidines for their anti-inflammatory, antinociceptive, and cyclooxygenase-2 Inhibition. *Chem. Biol. Drug Des.* **91**, 338–343 (2018).
28. Chainoglou, E. & Hadjipavlou-Litina, D. Curcumin in health and diseases: Alzheimer's disease and curcumin analogues, derivatives, and hybrids. *Int. J. Mol. Sci.* **21**, 1975 (2020).
29. Kabir, E., Noyon, K. & Md., Hossain, A. Synthesis, biological and medicinal impacts of metalodrugs: A study. *Results Chem.* **5**, 100935 (2023).
30. Dralle Mjos, K. & Orvig, C. Metalodrugs in medicinal inorganic chemistry. *Chem. Rev.* **114** (8), 4540–4563 (2014).
31. Ornelas, C. & Astruc, D. Ferrocene-Based Drugs, delivery nanomaterials and Fenton mechanism: state of the art, recent developments and prospects. *Pharmaceutics* **15**, 2044 (2023).
32. Shoukat, H. & Altaf, A. A. A. Badshah. *Advances in Metalodrugs: Preparation and Applications in Medicinal Chemistry* (Eds. ul-Islam, S., Hashmi, A. A., Khan, S. A.). 115–136 (Scrivener Publishing LLC, 2020).
33. Snegur, L. V. Modern trends in bio-organometallic ferrocene chemistry. *Inorganics* **10**, 226 (2022).
34. La Manna, S. et al. Enhancers of amyloid aggregation: novel ferrocene-based compounds selective toward amyloid models. *Inorg. Chem. Front.* **11**, 6577–6587 (2024).
35. Yao, P. et al. Ferrocene-modified peptides as inhibitors against insulin amyloid aggregation based on molecular simulation. *J. Mater. Chem. B.* **8**, 3076–3086 (2020).
36. Zhang, L. et al. Kinetic studies of inhibition of the A β (1–42) aggregation using a ferrocene-tagged β -sheet breaker peptide. *Anal. Biochem.* **434** (2), 292–299 (2013).
37. Beheshti, S., Martic, S. & Kraatz, H. B. Electrochemical signal-on reporter for amyloid aggregates. *ChemPhysChem* **13**, 542–548 (2012).
38. Poje, G. et al. Unveiling the antiglioblastoma potential of harmicins, harmine and ferrocene hybrids. *Acta Pharm.* **74** (4), 595–612 (2025).
39. Vessi res, A. et al. Heterogeneity of response to iron-based metalodrugs in glioblastoma is associated with differences in chemical structures and driven by FAS expression dynamics and transcriptomic subtypes. *Int. J. Mol. Sci.* **22**, 10404 (2021).
40. Peter, S. & Aderibigbe, B. A. Ferrocene-based compounds with antimalaria/anticancer activity. *Molecules* **24**, 3604 (2019).
41. Lain , A-L. et al. Inhibition of ectopic glioma tumor growth by a potent ferrocenyl drug loaded into stealth lipid nanocapsules. *Nanomed. : Nanotechnol Biol. Med.* **10**, 1667–1677 (2014).
42. de Oliveira, A. C. et al. Biological evaluation of twenty-eight ferrocenyl tetrasubstituted olefins: cancer cell growth inhibition, ROS production and hemolytic activity. *Eur. J. Med. Chem.* **46**, 3778–3787 (2011).
43. Kova , V. et al. Novel ferrocene-containing pyrazole analogs of curcumin: Synthesis, characterization, antioxidant activity, cyclic voltammetry, and in vitro biological evaluation. *Appl. Organometal Chem.* **39**, e7753 (2025).
44. Edison, A. S. & Schroeder, F. C. *Comprehensive Natural Products II, Chemistry and Biology* (Eds. Mander, L., Liu, H.-W.). Vol. 9. 169–196 (Elsevier, 2009).
45. Sipo ova, K. et al. Inhibition of amyloid fibril formation and disassembly of pre-formed fibrils by natural polyphenol Rottlerin. *BBA - Proteins Proteom.* **1867** (3), 259–274 (2019).
46. LeVine 3rd, H. Thioflavine T interaction with synthetic alzheimer's disease beta-amyloid peptides: detection of amyloid aggregation in solution. *Prot. Sci.* **2**, 404–410 (1993).
47. Groenning, M. et al. Binding mode of thioflavin T in insulin amyloid fibrils. *J. Struct. Biol.* **159**, 483–497 (2007).
48. Vus, K. et al. Thioflavin T derivatives for the characterization of insulin and lysozyme amyloid fibrils in vitro: fluorescence and quantum-chemical studies. *J. Lumin.* **159**, 284–293 (2015).
49. Sulatsky, M. I. et al. Effect of the fluorescent probes ThT and ANS on the mature amyloid fibrils. *Prion* **14** (1), 67–75 (2020).
50. Reinke, A. A. & Gestwicki, J. E. Structure–activity relationships of amyloid Beta-aggregation inhibitors based on curcumin: influence of linker length and flexibility. *Chem. Biol. Drug Des.* **70**, 206–215 (2007).
51. Jakubowski, J. M. et al. Interactions between curcumin derivatives and amyloid- β fibrils: insights from molecular dynamics simulations. *J. Chem. Inf. Model.* **60**, 289–305 (2020).
52. Orteca, G. et al. Curcumin derivatives and A β -fibrillar aggregates: an interactions' study for diagnostic/therapeutic purposes in neurodegenerative diseases. *Bioorg. Med. Chem.* **26** (14), 4288–4300 (2018).
53. Nath, S. et al. Hydroxy-porphyrin as an effective, endogenous molecular clamp during early stages of amyloid fibrillization. *Chem. Asian J.* **16**, 3931–3936 (2021).
54. Sipo ova, K. et al. Biocompatible zeolite-dye composites with anti-amyloidogenic properties. *Int. J. Biol. Macromol.* **251**, 126331 (2023).
55. Ferrari, E. et al. Vitro study on potential pharmacological activity of curcumin analogues and their copper complexes. *Chem. Biol. Drug Des.* **89** (3), 411–419 (2017).
56. Pevna, V. et al. Photobiomodulation and photodynamic therapy-induced switching of autophagy and apoptosis in human dermal fibroblasts. *J. Photochem. Photobiol B.* **234**, 112539 (2022).
57. Pevna, V., Wagn eres, G. & Huntosova, V. Autophagy and apoptosis induced in U87 MG glioblastoma cells by hypericin-mediated photodynamic therapy can be photobiomodulated with 808 nm light. *Biomedicines* **9**, 1703 (2021).
58. Schleinkofer, K., Wang, T. & Wade, R. C. *Encyclopedic Reference of Genomics and Proteomics in Molecular Medicine*. 1149–1153 (Springer, 2006).
59. Georgiou, N. et al. Conformational properties of new thiosemicarbazone and thiocarbohydrazone derivatives and their possible targets. *Molecules* **27** (8), 2537 (2022).

60. Paravastu, A. K. et al. Molecular structural basis for polymorphism in Alzheimer's β -amyloid fibrils. *Proc. Natl. Acad. Sci.* **105**(47), 18349–18354 (2008).
61. Bikadi, Z. & Hazai, E. Application of the PM6 semi-empirical method to modeling proteins enhances docking accuracy of AutoDock. *J. Cheminform.* **1** (1), 1–16 (2009).
62. Leonis, G. et al. Computational and spectroscopic analysis of the Quercetin encapsulation in (2HP- β -CD)2 and (2,6Me- β -CD)2 complexes. *J. Mol. Struct.* **1294** (P2), 136430 (2023).
63. Frisch, M. J. et al. *Gaussian 16, Revision B.01*. (Gaussian 09; 2016).
64. Siposova, K. et al. The intriguing dose-dependent effect of selected amphiphilic compounds on insulin amyloid aggregation: focus on a cholesterol-based detergent, Chobimalt. *Front. Mol. Biosci.* **9**, 955282 (2022).
65. Viet, M. H. et al. In Silico and in vitro study of binding affinity of tripeptides to amyloid β fibrils: implications for Alzheimer's disease. *J. Phys. Chem. B.* **119**, 5145–5155 (2015).

Acknowledgements

The authors also acknowledge to ZEISS company for support with super-resolution microscopy using Airyscan system.

Author contributions

V.K.: Methodology, Acquisition, analysis, and interpretation of data (compound synthesis and characterization); Funding acquisition; V. H.: Methodology, Acquisition, analysis, and interpretation of data (supervised biocompatibility and biodistribution studies), participated in original draft writing; Viktoria Fedorova: Investigation, microscopy; N. G.: docking study; Z. L.: Investigation, SMLM microscopy; Software; F.-C. C.: Methodology, Investigation, Software, Formal analysis; S.-J. C.: Formal analysis; F. D.: Investigation; compounds synthesis; K. S.: Conceptualization, methodology, investigation, writing - original draft; Funding acquisition; Review & editing.

Funding

This work has been supported by the Croatian Science Foundation project number HRZZ-IP-2020-02-9162 and by grants from SAS-NSTC-JRP-2024-03_SUPRA-SIGHT and SAS-MOST JRP 2021/2 (AZCAI), Slovak Grant Agency VEGA (No. 2/0034/22), and by the PhytoAPP EU framework (2021–2026). The PhytoAPP Project has received funding from the European Union's Horizon 2020 Research and Innovation programme under the Marie Skłodowska-Curie Grant Agreement No.101007642. Views and opinions expressed are however those of the author(s) only and do not necessarily reflect those of the European Union or the European Research Executive Agency. Neither the European Union nor the granting authority can be held responsible for them. The work was also funded by the EU NextGenerationEU through the Recovery and Resilience Plan for Slovakia under the project No. 09-I02-03-V01-00021.

Declarations

Competing interests

The authors declare no competing interests.

Additional information

Supplementary Information The online version contains supplementary material available at <https://doi.org/10.1038/s41598-025-23467-0>.

Correspondence and requests for materials should be addressed to K.S.

Reprints and permissions information is available at www.nature.com/reprints.

Publisher's note Springer Nature remains neutral with regard to jurisdictional claims in published maps and institutional affiliations.

Open Access This article is licensed under a Creative Commons Attribution-NonCommercial-NoDerivatives 4.0 International License, which permits any non-commercial use, sharing, distribution and reproduction in any medium or format, as long as you give appropriate credit to the original author(s) and the source, provide a link to the Creative Commons licence, and indicate if you modified the licensed material. You do not have permission under this licence to share adapted material derived from this article or parts of it. The images or other third party material in this article are included in the article's Creative Commons licence, unless indicated otherwise in a credit line to the material. If material is not included in the article's Creative Commons licence and your intended use is not permitted by statutory regulation or exceeds the permitted use, you will need to obtain permission directly from the copyright holder. To view a copy of this licence, visit <http://creativecommons.org/licenses/by-nc-nd/4.0/>.

© The Author(s) 2025